water

MDPI

*Article*

# Integrated Assessment of the Hydrogeochemical and Human Risks of Fluoride and Nitrate in Groundwater Using the RS-GIS Tool: Case Study of the Marginal Ganga Alluvial Plain, India

**Dev Sen Gupta [1], Ashwani Raju [2,*], Abhinav Patel [3], Surendra Kumar Chandniha [4], Vaishnavi Sahu [5], Ankit Kumar [2], Amit Kumar [6,*], Rupesh Kumar [7] and Samyah Salem Refadah [8]**

1 Defence Geoinformatics Research Establishment, Defence Research & Development Organisation, Sector-37A, Chandigarh 160036, India
2 Remote Sensing & GIS Laboratory, Department of Geology, Institute of Science, Banaras Hindu University, Varanasi 221005, Uttar Pradesh, India; ankitgeo@bhu.ac.in
3 Hydrogeology Laboratory, Department of Geology, Institute of Science, Banaras Hindu University, Varanasi 221005, Uttar Pradesh, India; abhinav.geology17@bhu.ac.in
4 College of Agricultural Engineering and Technology & Research Station, Indira Gandhi Krishi Vishwavidyalaya, Raipur 495334, Chhattisgarh, India; surendra.chandniha@igkv.ac.in
5 Department of Botany, Institute of Science, Banaras Hindu University, Varanasi 221005, Uttar Pradesh, India; vaishusahu682@gmail.com
6 School of Hydrology and Water Resources, Nanjing University of Information Science and Technology, Nanjing 211544, China
7 Jindal Global Business School (JGBS), Jindal Global University, O. P, Sonipat 131029, Haryana, India; rupesh.kumar@jgu.edu.in
8 Department of Geography and GIS, Faculty of Arts and Humanities, King Abdulaziz University, Jeddah 21589, Saudi Arabia; srefadah@kau.edu.sa
* Correspondence: ashwani.geo@bhu.ac.in (A.R.); amitkdah@nuist.edu.cn (A.K.)



**Citation:** Gupta, D.S.; Raju, A.; Patel, A.; Chandniha, S.K.; Sahu, V.; Kumar, A.; Kumar, A.; Kumar, R.; Refadah, S.S. Integrated Assessment of the Hydrogeochemical and Human Risks of Fluoride and Nitrate in Groundwater Using the RS-GIS Tool: Case Study of the Marginal Ganga Alluvial Plain, India. *Water* **2024**, *16*, 3683. https://doi.org/10.3390/w16243683

Academic Editors: Andrea G. Capodaglio, Liangping Li and Guanxing Huang

Received: 19 November 2024
Revised: 10 December 2024
Accepted: 17 December 2024
Published: 20 December 2024



**Abstract:** Groundwater contamination with sub-lethal dissolved contaminants poses significant health risks globally, especially in rural India, where access to safe drinking water remains a critical challenge. This study explores the hydrogeochemical characterization and associated health risks of groundwater from shallow aquifers in the Marginal Ganga Alluvial Plain (MGAP) of northern India. The groundwater chemistry is dominated by Ca-Mg-$CO_3$ and Ca-Mg-Cl types, where there is dominance of silicate weathering and the ion-exchange processes are responsible for this solute composition in the groundwater. All the ionic species are within the permissible limits of the World Health Organization, except fluoride ($F^-$) and nitrate ($NO_3{}^-$). Geochemical analysis using bivariate relationships and saturation plots attributes the occurrence of $F^-$ to geogenic sources, primarily the chemical weathering of granite-granodiorite, while $NO_3{}^-$ contaminants are linked to anthropogenic inputs, such as nitrogen-rich fertilizers, in the absence of a large-scale urban environment. Multivariate statistical analyses, including hierarchical cluster analysis and factor analysis, confirm the predominance of geogenic controls, with $NO_3{}^-$-enriched samples derived from anthropogenic factors. The spatial distribution and probability predictions of $F^-$ and $NO_3{}^-$ were generated using a non-parametric co-kriging technique approach, aiding in the delineation of contamination hotspots. The integration of the USEPA human health risk assessment methodology with the urbanization index has revealed critical findings, identifying approximately 23% of the study area as being at high risk. This comprehensive approach, which synergizes geospatial analysis and statistical methods, proves to be highly effective in delineating priority zones for health intervention. The results highlight the pressing need for targeted mitigation measures and the implementation of sustainable groundwater management practices at regional, national, and global levels.

**Keywords:** fluoride and nitrate; Ganga Alluvial Plain; kriging; USEPA approach; mitigation and adaptation

## 1. Introduction

Groundwater constitutes about 30% of global freshwater resources and is vital for agriculture, drinking water, and industry. India holds 4% of global freshwater but hosts 17% of the world's population, thereby facing severe water scarcity [1]. Over 25% of global groundwater use occurs in India, but excessive extraction has led to issues like depletion, pollution, and saltwater intrusion [2,3]. Per capita water availability, currently at 1486 $m^3$, is expected to drop below 1140 $m^3$ by 2050, exacerbating the crisis. Climate change further intensifies this challenge, with groundwater depletion rates projected to triple by 2041–2080, due to rising irrigation demands [4–6]. The contamination of groundwater with fluoride is one of the primary global issues. It has been previously estimated that in 25 nations, a huge percentage of the population, numbering around 200 million people, suffers from fluorosis globally, and the causes behind it have been attributed to the contamination of groundwater with fluoride, including in India [7,8]. All countries are more prone to fluoride exposure due to the consumption of fluoride-rich groundwater. Fluoride is the most electronegative element, which occurs as fluoride ions ($F^-$), and is commonly associated with natural processes for its release in the groundwater system [9–11]. Fluoride is a basic element in the growth of teeth and bones; the presence of fluoride ensures strength, but in excess, it causes serious health issues.

Fluoride enters the human body through both anthropogenic and geogenic methods, with geogenic contributions being more prominent in India [1,7]. Geogenic sources include the weathering process, leaching, fluoride-bearing mineral dissolution, the exchange of ions, rock–water interactions, and evaporative enrichment [10,11]. The anthropogenic sources, namely, industrial activities, coal burning, and phosphate fertilizers, increase the concentrations of fluoride in groundwater. Sulfate and nitrate are two other potentially hazardous ions found in fertilizer products. Fluoride keeps teeth healthy (the prevention of dental caries, dental enamel construction, and the establishment of bone minerals). Fluoride concentrations below 0.5 mg/L in drinking water can lead to dental issues such as cavities, diminished bone mineralization, and a lack of dental enamel production.

Conversely, concentrations exceeding 1.5 mg/L pose significant health risks, including dental fluorosis and skeletal fluorosis, which can severely impair bone and joint health [12–14]. The fluoride content greatly depends on the mineralogy of the host lithology, which dictates the level of its concentration in groundwater [2,5,15–23]. Fluoride contamination in aquifers arises due to rock erosion and exposure to minerals rich in fluoride. High fluoride concentrations in groundwater are expected in calcium-deficient sodium bicarbonate-type water. The alkaline etiquette of water promotes the conversion of fluorite ($CaF_2$) to fluoride. The main sources of Fluoride include rock minerals, namely, calcium fluoride [$CaF_2$], fluorapatite [$Ca_5(PO_4)3F$], and cryolite [$Na_3AlF_6$], whereas anthropogenic sources contain coal fly ash, petrol refinery waste, enhanced brick kilns dust, and extreme use of chemical fertilizers [23,24].

Fluoride and nitrate are significant ionic constituents in groundwater that influence its suitability for drinking. Fluoride primarily originates from geogenic sources, such as the dissolution of fluoride-rich minerals, while nitrate is often introduced through anthropogenic activities, including the use of agricultural fertilizers, domestic effluents, dairy operations, and nearby waste treatment plants [8,25–28]. According to USEPA, the recommended limit for nitrate in drinking water is 10 mg/L, while the BIS allows up to 45 mg/L, and the WHO sets the maximum at 50 mg/L. Recently, nitrate contamination has become a global issue, affecting most of those Asian and African countries where the uncontrolled use of fertilizers has been observed [29]. Nitrate contamination reduces the pH of water, making it acidic. Its hazardous effects cause methemoglobinemia and the creation of nitrosamine compounds in the human body. Methemoglobinemia disease is a critical condition that may sometimes prove carcinogenic and otherwise hazardous to health; it can be connected to cardiac dysrhythmias, circulatory failure, oxygen deprivation with cyanosis, and central nervous system (CNS)-related effects [27].

The Mahoba district in the Bundelkhand gneissic complex is characterized by granite rock geology, meaning that the weathering of granite rocks leads to the contamination of groundwater with fluoride. In this region, fluoride and nitrate are identified as the primary contaminants, posing substantial risks to human health. The human health risk assessment (HRA) model, as outlined by the USEPA (2014) [30], was employed to evaluate the health impacts of these contaminants via multiple exposure pathways. Geographic information systems (GIS), supported by statistics-based techniques like interpolation and regression analysis, were used to predict contaminant concentrations at unsampled locations. These methods draw upon established techniques [31–37] to generate spatially explicit risk maps. By integrating the predicted contaminant distribution with human census data, the study effectively visualized the spatial extent of health risks [12,13,38,39]. These vivid risk maps highlight hotspots, aiding in targeted mitigation and management strategies for groundwater quality improvement in the region. One tool of Arc GIS, named 'geostatistical analyst', is an extension module that has been used for exploratory data analysis, cross-validation purposes, the semivariogram model, and establishing the distribution pattern of groundwater contaminant concentrations. Kriging is a prediction tool based on statistical analysis that defines the stochastic theory for evaluating the spatial behavior of geographic data [22]. Ordinary kriging (OK) is used to create the spatial distribution of water quality and contaminants in the study area, whereas indicator kriging (IK) is used to calculate the probability of contaminants. The sub-lethal elements occurring at the local and/or regional scales put human health "at risk". HRA evaluates the potential exposure and adverse effects of toxic substances on the population through risk evaluation, exposure assessment, and hazard characterization (IPCS 2004). The globally adopted USEPA (2014) HRA model serves as a framework to assess the impact of contaminants on human health. Researchers worldwide have utilized these policies and guidelines to highlight the human health risks posed by environmental contaminants [40–48].

Fluoride and nitrate contamination in groundwater is a global concern, and the Bundelkhand region faces this issue, along with significant water depletion [33–35,49–51]. The majority of the population relies on shallow, unconfined aquifers for drinking water, exacerbating their vulnerability due to widespread poverty [14,52,53]. Exposure to nitrate and fluoride and their impacts on human health is important to understand in the present context. This research explores the hydrogeochemical evolution of the groundwater samples collected, with special reference to fluoride and nitrate contaminants. Different statistical approaches have been used to decipher the inter-correlation of hydrogeochemical parameters spatially, and a human health risk assessment was carried out using the USEPA approach. Research gaps on the Marginal Ganga Alluvial Plain include inadequate spatial and temporal assessments of groundwater contamination by fluoride and nitrate, particularly under the influence of agricultural and industrial activities. Yet, there has been limited exploration of contamination from combined geogenic and anthropogenic factors. The proper isotopic studies have not been carried out to understand source-related issues in further detail. Additionally, health risk assessments that consider local socio-economic and demographic conditions are scarce, hindering effective mitigation strategies. The present study seeks to develop a comprehensive framework by integrating hydrogeochemical analysis, multivariate statistical techniques, and the urbanization index to address groundwater contamination challenges in the sparsely populated regions of Bundelkhand. Furthermore, the application of non-parametric co-kriging for the spatial prediction of fluoride ($F^-$) and nitrate ($NO_3^-$) contamination represents a significant methodological advancement, enabling the precise delineation of high-risk hotspots and enhancing the effectiveness of targeted mitigation strategies. The research objectives are to: (i) investigate the chemical processes influencing groundwater quality, focusing on fluoride and nitrate pollution, (ii) elucidate the patterns of fluoride and nitrate distribution using multivariate statistical approaches and geostatistical modeling, and (iii) quantify exposure risks to the population through the Human Health Risk Assessment framework, applying probabilistic models to predict contaminant impacts effectively.

## 2. Materials and Methods

### *2.1. Study Area*

Mahoba, a district of Bundelkhand region, Uttar Pradesh, is a part of the Marginal Ganga Alluvial Plain (MGAP), situated between the Indo-Gangetic Plain to the north and the Vindhyan Range to the south (Figure 1). The total geographic area of this district is about 2884 sq. km. Mahoba lies in the geographic location of N 25° 01′ 30″ to N 25° 39′ 40″ and E 79° 15′ 00″ to E 80° 10′ 30″. The normal decadal average rainfall in the monsoon season for Mahoba is 753 mm, whereas decadal non-monsoon rainfall has been recorded at 76 mm [52]. The four area blocks (Panwari, Charkhari, Kabrai, and Jaitpur) are drained by certain rivers, namely, the Dhasan, Urmil, Birma, and Arjun. May has the highest temperatures, shooting up to 50 °C, and January is the coldest month, with a temperature of less than 4 °C [54].

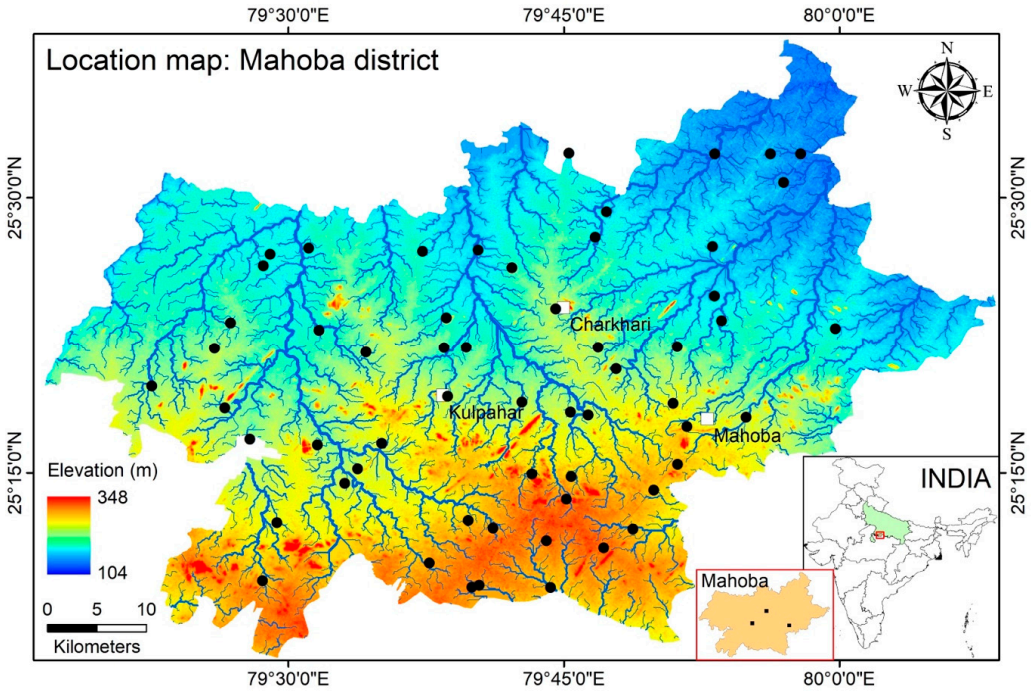


**Figure 1.** Study area map, with sampling locations (black circle) in the Marginal Ganga Alluvial Plain.

The Mahoba district in the Bundelkhand consists of granite, granodiorite, granitic gneisses, and dolerite, due to the presence of the Bundelkhand Massif Terrain (Figure 2). Granite rocks are a type of intrusive igneous rock composed mostly of quartz, mica, and alkali feldspar. The depth-to-water level in the Mahoba command area for the pre-monsoon season is 8.75 mbgl, while for the post-monsoon season, it is 6.29 mbgl [52]. The groundwater level is low in the Mahoba district because the district mainly comprises the hard rock formation of the Bundelkhand Massif. The rocks are massive; therefore, rainfall does not percolate the rocks [55]. However, some water can percolate through the cracks in the rocks, which helps to keep the water level stable. The occurrence of groundwater in this terrain is extremely uncertain, due to its hilly and rugged terrain. Fluoride, nitrate, sulfate, and calcium are the primary contaminants in the groundwater. Agriculture is the main source of economic activity because a large percentage of the population lives in rural areas. Irrigation practice depends on groundwater (60%) and surface water (40%) [54]. The land use/land cover (LULC) regulates the infiltration behavior of any region, and the LULC map of the study area shows the major cover of agriculture in the region (Figure 3). The shortage of water bodies and streams results in an insufficient amount of water for irrigation throughout the year. Water scarcity, the ingestion of contaminated water, unhygienic sanitation, and several health issues are common problems facing the people of the district.

Additionally, improper solid waste management and landfilling lead to the contamination of groundwater.

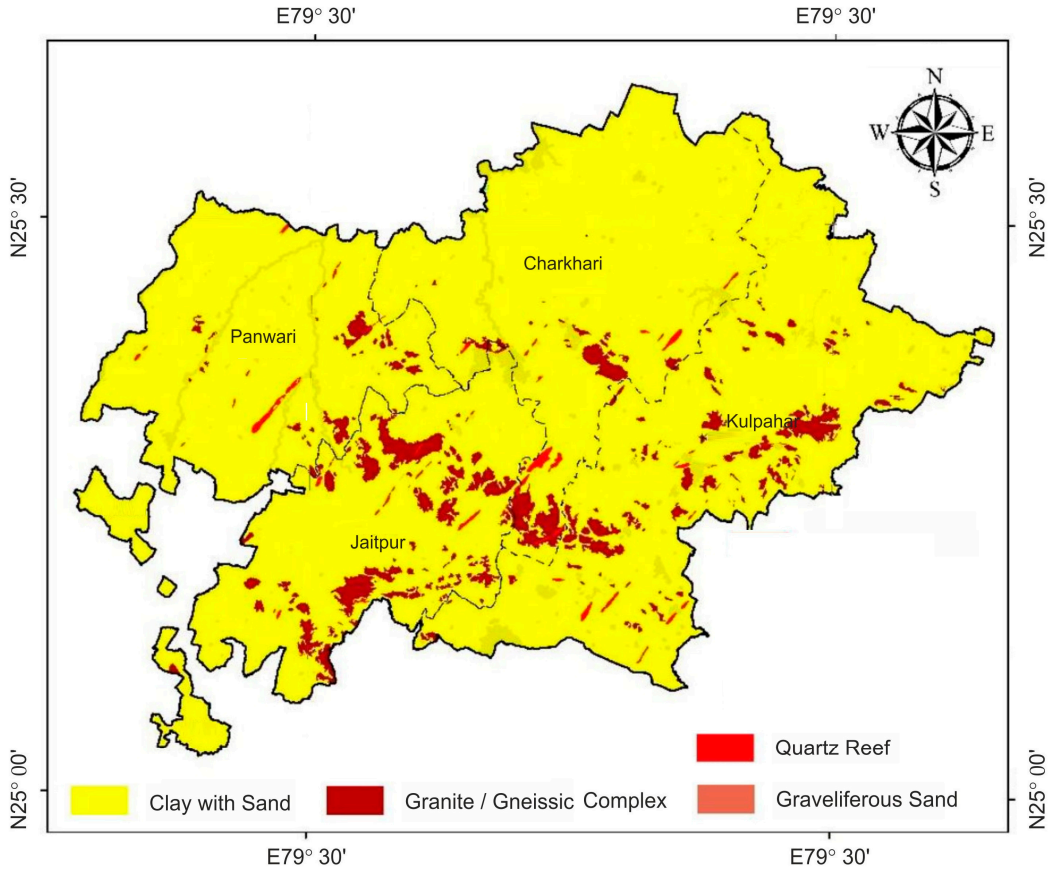


**Figure 2.** Lithological map of the study area, highlighting the major geology of the region.

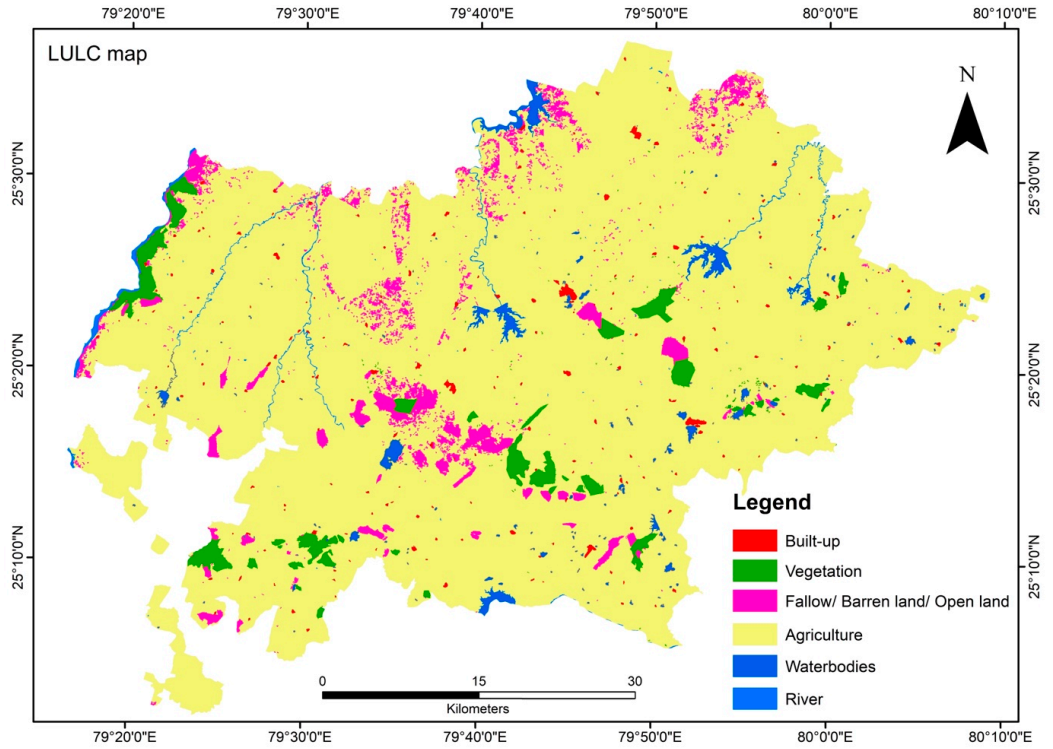


**Figure 3.** LULC map of the study area, highlighting the major land cover in the region.

### 2.2. Groundwater Sample Collection

Groundwater sampling ($n$ = 60) was planned to be one sample from every 60 grids divided equally, but, in the field, this pattern was modified based on groundwater source availability (see the Supplementary Materials (SM: Table S1)). Two sets of groundwater samples taken from the India Mark-II samples after filtering (with 0.20 µm Millipore membrane syringe filters) were collected in pre-washed HDPE bottles for major ions and trace metals, respectively. To each 100 mL of collected samples, ultra-pure $HNO_3$ was added for the preservation of heavy metals. On-site parameters such as coordinates, electrical conductivity (µS/cm), and pH (Consort C831) were measured through portable meters [1]. The main cations ($Ca^{2+}$, $K^+$, $Mg^{2+}$, $Na^+$) and anions ($NO_3{}^-$, $F^-$, $Cl^-$, $SO_4{}^{2-}$) in the laboratory samples were evaluated in an ion chromatograph (model: Dual channel 930 Compact IC Flex ChS/PP) and via ICP-MS for heavy metals (Fe, Cr, Cu, As, Bi, Co, Al, and Pb). The instruments were verified for correct calibration, and the results were then cross-checked using the charge balance error (CBE) within ± 5%. The results showed that many samples exceeded the permissible limits prescribed by the WHO [56] and BIS [57].

### 2.3. Bivariate and Ternary Plots

To analyze the hydrogeochemical evolution of groundwater and the mechanisms driving the release of ionic species, various molar ratios and bivariate plots were utilized. Classical hydrogeochemical tools, such as Gibbs plots [58], were employed to identify the dominant processes controlling water chemistry, including evaporation, rock–water interactions, and precipitation. Chadha's (1999) [59] rectangular diagram was also applied to classify groundwater types and elucidate the prevailing weathering processes shaping the ionic composition in the study area. These analytical approaches provide insights into the geochemical behavior of groundwater and the factors influencing its quality.

### 2.4. Multivariate Statistical Approach

The study addresses the complexity of analyzing groundwater quality across multiple sampling sites with numerous hydrochemical parameters, which constitutes a multivariate problem [9,10,35,60]. To simplify this complexity, factor analysis (FA), which is a dimension reduction technique, and hierarchical cluster analysis (HCA) were employed to group those sampling sites with similar underlying hydrochemical characteristics, enabling the classification of groundwater samples based on shared underlying processes. These statistical approaches facilitate the systematic interpretation of hydrogeochemical data and the identification of dominant contamination sources [48,61,62]. Both FA and HCA were normalized and standardized to a z-score [11]. Barlett's test of sphericity and KMO were applied, followed by a varimax rotation for FA, which yielded 5 PCs (eigenvalues > 1). HCA is a very good correlation technique for understanding the factors affecting the hydrogeochemistry seen in this study area. In HCA, multivariate similarity or dissimilarity has been performed using Ward's (1963) [63] method. This technique helps in the clustering of samples, showing interrelation between all the samples using the variance approach [2].

### 2.5. Geostatistical Modeling Using 'Indication Kriging'

The dissolved elemental concentration of $F^-$ and $NO_3{}^-$ has been considered herein as a random variable [Z (x_i); iε {1. . .n}] for spatial interpolation. Each random variable has been used to prepare a regional database transformed into a smooth continuous surface using 'kriging'. The output is in the form of a thematic map, showing the spatial distribution of $F^-$ and $NO_3{}^-$. Kriging, a geostatistical prediction model, explains the distribution of a random variable (z) in a geographical space (reference). Kriging adopts the regionalized variable theory to determine the spatial continuity of the random variable (z) in a framework of linear model expressed by the function of (a) the structural component spatial trend or

mean, [m($x_i$)], (b) a spatially autocorrelated random variable (regionalized, [ε′(x_i)]), and (c) random noise (stochastic variation, independent of a location, (ϵ) (Equation (1)).

$$z(x_i) = m(x_i) + \varepsilon' x_i + \epsilon \quad (1)$$

The spatial autocorrelation $[\varepsilon'(x_i)]$ is the random variable dependency, based on their spatial arrangement $[z(x_i)]$, using semivariance $[\gamma_i(h)]$. Semivariance is half the variance between all the possible random variables (average square difference between the variables, i.e.,$[z(x_i)]$ and $[z(x_i + h)]$, in a space separated by a lag distance $(h)$ (Equation (2)):

$$\gamma(h) = \frac{1}{2n(h)} \sum_{i=1}^{n(h)} \{z(x_i) - z(x_i + h)\}^2 \quad (2)$$

where $\gamma(h)$ is semivariance, $[z(x_i)]$ is the value at the location $(x_i)$ of a known variable, n is the number of pairs of sample point $z(x_i)$, and "h" represents the distance (lag distance) between a pair of points $(x_i)$ and $(x_i + h)$.

Semivariance transforms the random variable into a continuous raster surface by exploring its spatial behavior when distributed in a regional space, using the parameters derived from the semivariogram plot. These parameters, i.e., nugget ($C_o$), sill ($C_o$ + $C_1$), and range ($C_2$), were estimated from the best-fitting semivariogram model. Nugget defines the highest degree of autocorrelation; sill is the point where the best-fit curves level off, and range is the lag distance over which random variables are spatially dependent. The semivariance $[\gamma(h)]$ derived from the best-suited semivariogram model is later substituted into Equation (3) to derive the weights $(\lambda_i)$.

$$\sum_{i=1}^{n} \lambda_i \gamma(x_i) + \varepsilon = \gamma(x_i) \quad (3)$$

Finally, spatial prediction (z′) at an unknown location is estimated from the known variable $[z(x_i)]$ by introducing a weight $(\lambda_i)$ derived from Equations (3) and (4).

$$z'(x_0) = \sum_{i=1}^{n} \lambda_i z(x_i) \quad (4)$$

However, to obtain probability-based predictions from continuous or categorical data, a more advanced approach called indicator kriging (IK) is used. It transforms the data into binary indicator codes based on the desirable thresholds, thereby minimizing the influence of outliers in the data. Indicator kriging uses a desirable threshold to transform the random variables $[z(x_i)]$ into the indicator codes $[I(x_i) = 0 \; or \; 1]$ for spatial autocorrelation. The indicator codes were considered to be 0 if the concentration of the random variable was below the desirable threshold: $[z(x_i) \geq z_{th}]$, otherwise 1. Later, spatial autocorrelation between the indicator codes used semivariance $[\gamma_i(h)]$, derived from the best-fitting semivariogram plot (Equation (5)).

$$\gamma_i(h) = \frac{1}{2n(h)} \sum_{i=1}^{n(h)} \left\{ x(x_i; z_{th}) - I(x_i + h; z_{th}) \right\}^2 \quad (5)$$

Finally, the derived semivariance $[\gamma_i(h)]$ is integrated with a Lagrange multiplier to derive the weights $(\lambda_i)$, which are later used to generate predicted probability estimates varying in class from 0 to 1, using Equation (6).

$$I'(x_0; z_{th}) = \sum_{i=1}^{n} \lambda_i I(x_0; z_{th}) \quad (6)$$

The suitability of the selected semivariogram model is tested using a cross-validation plot generated between the predicted and measured probability values. In addition, the maximum percentage of indicator values is modeled by the semivariogram, which is

calculated by Equation (7); here, $\gamma_i(h)$ is the total semivariance or sill, and $\varepsilon(x_i)$ is an error related to the nugget.

$$Maximum\ Semivariance\ \% = \frac{[\ \gamma_i(h)] - [\varepsilon(x_i\ )]}{[\gamma_i\ \ (h)]} \times 100 \quad (7)$$

*2.6. Human Health Risk Assessment Using the USEPA Approach*

The study area, which has been identified as water-deficient, faces challenges such as irregular monsoonal rainfall, reduced recharge capacity, declining water levels, and intensified water–rock interactions, leading to elevated contaminant levels in aquifers. Inadequate sanitation and water treatment render the available water unsuitable for drinking, necessitating an assessment of the health risks from exposure to dissolved ions. The human health risk assessment (HRA) evaluates the population risks associated with such exposures. To observe human health at risk, a widely known empirical model defined by USEPA has been used in this article. The empirical model explains the relationship between dose response and human exposure in a contaminated environment. Humans can be exposed to a particular contaminant via three different routes, i.e., the direct ingestion of contaminated drinking water, absorption via the skin, and inhalation. Since the present approach involves the assessment of human health at risk from exposure to dissolved ionic concentrations in the drinking groundwater resources of the Mahoba area, a risk assessment for the direct intake (ingestion) of drinking water has been considered here. As the observed nitrate and fluoride levels are above the prescribed permissible limit, only these two substances have been considered in this USEPA-based empirical model. The derived estimates of potential health risks from exposure to fluoride and nitrate were combined with the human population dataset to determine the spatial extent of the exposure risk in a geographical space. The sequential formulation for USEPA-based human health risk assessment is as follows (Equation (8)):

$$CDI_w\ = \frac{C_w\ .IR.EF.ED}{BW.AT} \quad (8)$$

where CDI is the exposure dose (mg/kg/day) of the contaminants, Cw is the contamination of groundwater in mg/L, IR is the ingestion groundwater ratio (L/day), EF is the exposure frequency (365 days per year), ED is the exposure length (30 years), BW is a body weight (in kg) of approximately 60 kg, and AT denotes the average period of exposure (365 days).

To calculate the hazard quotient (HQ) using Equation (9), the estimated CDIs for individual components have been combined with the reference dose of a particular contaminant (RD). The values for fluoride were collected from the integrated risk information system, USEPA 2012, and are 0.007 mg/kg/day. When the HQ value is greater than 1, it means that the non-carcinogenic risk is greater than is permissible.

$$HQ_w\ = \frac{CDI_w}{RfD_w} \quad (9)$$

The hazard index (HI) is used to assess the risk of a specific diversity of interest after exposure to a mixture of chemicals. The HI values of fluoride and nitrate were calculated using Equation (10).

$$HI = HQ_{F-} + HQ_{NO3-} \quad (10)$$

Since the health risk assessment, as derived from the USEPA approach, is closely linked with the human population consuming drinking water, a close approximation of health risk estimates that is integrated with accounts of urbanization would give a precise distribution of human health at risk. The level of urbanization in the study area was assessed by integrating the harmonized night-time light (NTL) data from DMSP-OLS and VIIRS with a gridded population density dataset from CIESIN [19,64]. The NTL data represent urban intensity through night-time light emissions, but features like streetlights,

government workplaces, parks, etc., have no population during the night-time. To address this issue, the population density dataset is adjusted by assigning > 1,000,000 administrative unit counts to a unit pixel. However, this approach misrepresents low-population areas near urban centers by equating them with highly populated regions [6]. Thus, a combined analysis of NTL and CIESIN data using Equation (11) is employed for more accurate urban population estimates.

$$UI = \frac{(NTL_{rescale}) \times (PD_{rescale})}{Total\ Area} \quad (11)$$

To assess the human health risk in the studied region, the world gridded population datasets from the University of Columbia (census) were integrated with calculated HI values to create a risk map using Equation (12).

$$Human\ Health\ Risk\ Index\ (HHRI) = \frac{(UI) \times (HI)}{Total\ Area} \quad (12)$$

An overview of the methodology adopted in the present study is shown in Figure 4.

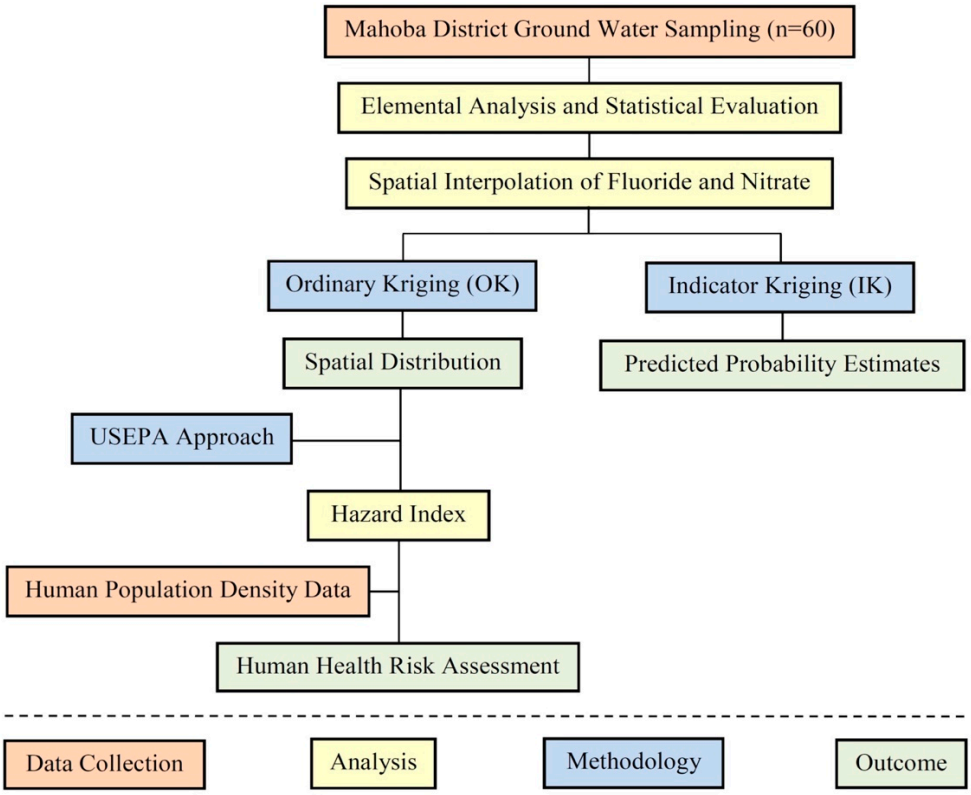


**Figure 4.** The methodology adopted for this study.

## 3. Results and Discussion

### *3.1. Hydro-Geochemistry and Water Type*

Most of the groundwater samples appeared to be moderately mineralized and did not appear to vary much in terms of their major ion chemistry across spatial scales, as reflected in their skewness values in Table 1. However, when compared with WHO standard, it is evident that 5%, 26.7%, and 43.3% of the groundwater samples for pH, $F^-$, and $NO_3^-$ exceeded the recommended levels in water for drinking purposes. The consumption of fluoride-rich groundwater in the long term may lead to various skeletal health ailments, while $NO_3^-$ poisoning leads to blue baby syndrome, which has been reported around the globe. Therefore, it is vital to understand the release mechanism of these inorganic contaminants, which have proved to be fatal to human life and may lead to socioeconomic instabilities. The hydrogeochemical facies analysis of groundwater is an

important technique using Chadha's (1999) rectangular plot, by which we understand the groundwater facies as being in four zones. Zone 1 corresponds to Ca-Mg-$HCO_3$ water types; this type of water facies generally results in recently recharged groundwater water. The most dominating water facies, as per the Chadha rectangular plot (Figure 5), is Ca-Mg-Cl, which describes groundwater with a considerably long residence time, thereby facilitating ion exchange processes in the aquifer system. The peculiar water type associated with the high $F^-$ value is Na-$HCO_3$, which shows the relationship between the release of $F^-$ and $Na^+$ under alkaline conditions from the silicate-bearing minerals found abundantly in the study area [65].

**Table 1.** Descriptive statistics of the various hydrochemical parameters and their comparison with the World Health Organization-recommended limit (WHO 2017).

| Parameter | Mean | Min | Max | Std. Dev | Skewness | WHO (2017) | % Exceeding |
|---|---|---|---|---|---|---|---|
| pH | 7.7 | 6.7 | 8.9 | 0.5 | 0.2 | 6.5–8.5 | 5.0 |
| EC (µS/cm) | 907.3 | 628.0 | 1247.0 | 131.8 | 0.0 | | |
| $CO_3^{2-}$ (mg/L) | 14.6 | 0.0 | 41.0 | 7.3 | 1.3 | | |
| $HCO_3^-$ (mg/L) | 206.7 | 107.0 | 380.0 | 58.2 | 0.3 | | |
| $F^-$ (mg/L) | 1.4 | 0.5 | 3.0 | 0.5 | 1.0 | 1.5 | 26.7 |
| $Cl^-$ (mg/L) | 95.2 | 19.7 | 215.0 | 35.2 | 1.3 | | |
| $SO_4^{2-}$ (mg/L) | 59.7 | 10.0 | 131.0 | 15.6 | 1.0 | 200–400 | |
| $NO_3^-$ (mg/L) | 55.6 | 20.1 | 118.1 | 27.2 | 0.9 | 50.0 | 43.3 |
| $Na^+$ (mg/L) | 70.6 | 37.5 | 97.8 | 16.5 | −0.1 | | |
| $K^+$ (mg/L) | 1.2 | 0.0 | 2.8 | 0.6 | 0.3 | 12.0 | |
| $Mg^{2+}$ (mg/L) | 25.6 | 5.3 | 40.2 | 7.6 | −0.5 | | |
| $Ca^{2+}$ (mg/L) | 68.2 | 41.1 | 89.9 | 11.8 | −0.1 | | |

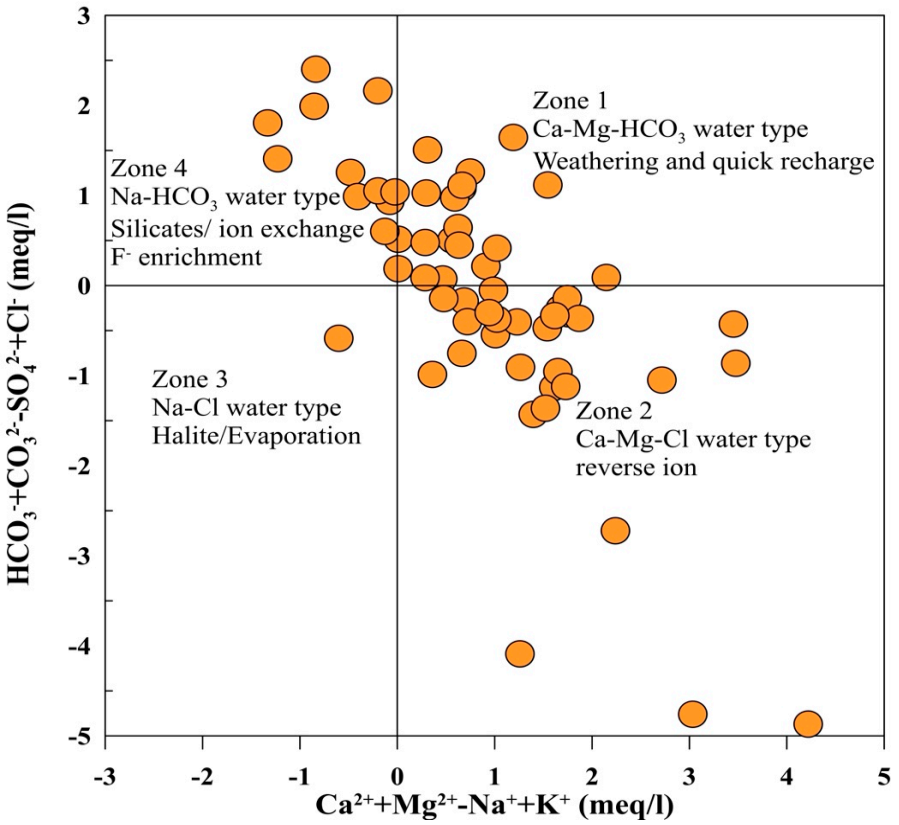


**Figure 5.** Chadha rectangular plot for various water types.

### 3.2. Solute Acquisition Processes

The source of solute in groundwater can generally be categorized as geogenic, anthropogenic, or natural-borne. The chemistry of groundwater evolves through various processes, including an interaction between the groundwater and aquifer matrix, human activities, or a combination of these factors [33]. When the alkalinity of groundwater is high, the hydroxyl ion readily replaces the fluoride ion in minerals such as mica, elite, and amphiboles, releasing F- into the groundwater [23]. Groundwater chemistry evolves due to the continuous interactions of recharging water and soil in the aquifer matrix, chemicals from anthropogenic activities, and other factors [33]. Furthermore, many sodium and bicarbonate minerals increase the concentration of fluoride in the groundwater. When calcium-rich groundwater transforms into sodium-rich groundwater, the probability of fluoride solubility increases [23]. Rock-dominant processes contribute the major ion contents to the groundwater samples for the present study. An increase in $Na^+ + K^+/Na^+K^+ + Ca^{2+}$ (Figure 6a,b) is the result of an increase in the concentration of monovalent cations due to the presence of silicate minerals in the aquifer matrix (Equations (13) and (14)).

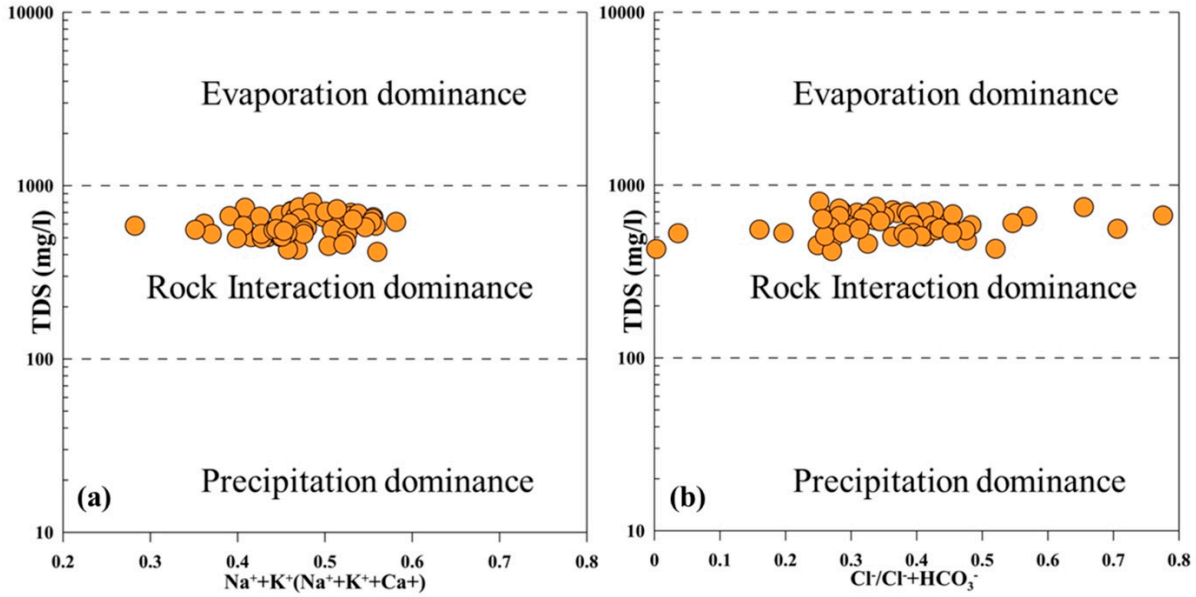


**Figure 6.** (**a**,**b**): Gibb's plot showing (**a**) the ratio between $(Na^+ + K^+)/(Na^+ + K^+ + Ca^{2+})$ as a function of TDS; (**b**) the ratio between $(Cl^- + NO^{3-})/(Cl^- + NO^{3-} + HCO^{3-})$ as a function of TDS.

The atmospheric input in the solute/salts dissolved in subsurface water can be understood by their ionic ratio to $Cl^-$ [47]. In the present setting, the mean ratios of $K^+/Cl^-$ and $Na^+/Cl^-$ of groundwater are 1.68 and 0.03, respectively, which are far higher than marine aerosols ($Na^+/Cl^-$ = 0.85 and $K^+/Cl^-$ = 0.017), showing solute derived from host rock rather than atmospheric direct input [1,3,46]. The $Na^+/Cl^-$ level for 86% of the groundwater samples is greater than 1, clearly demonstrating the presence of other sources of $Na^+$ than halite dissolution (Figure 7a). The molar ratio $Ca^{2+}/Mg^{2+}$ for 28% of the groundwater samples of >2 depicts the importance of silicate weathering. However, the significant samples fall within the molar ratio $(Ca^{2+}/Mg^{2+}) > 1 < 2$, which might be due to the prevalence of Ca-rich silicate minerals or the ion exchange process in the substratum. The contribution of monovalent cations to the total cation can be understood through the $Na^+ + K^+$ vs. total cation process (Figure 7b). A significant amount of the groundwater samples are clustered around the $Na^+ + K^+ = 0.5 \times$ total cation ($TZ^+$) calculation, identifying the source of these ions ($Na^+ + K^+$) as silicate weathering [66].

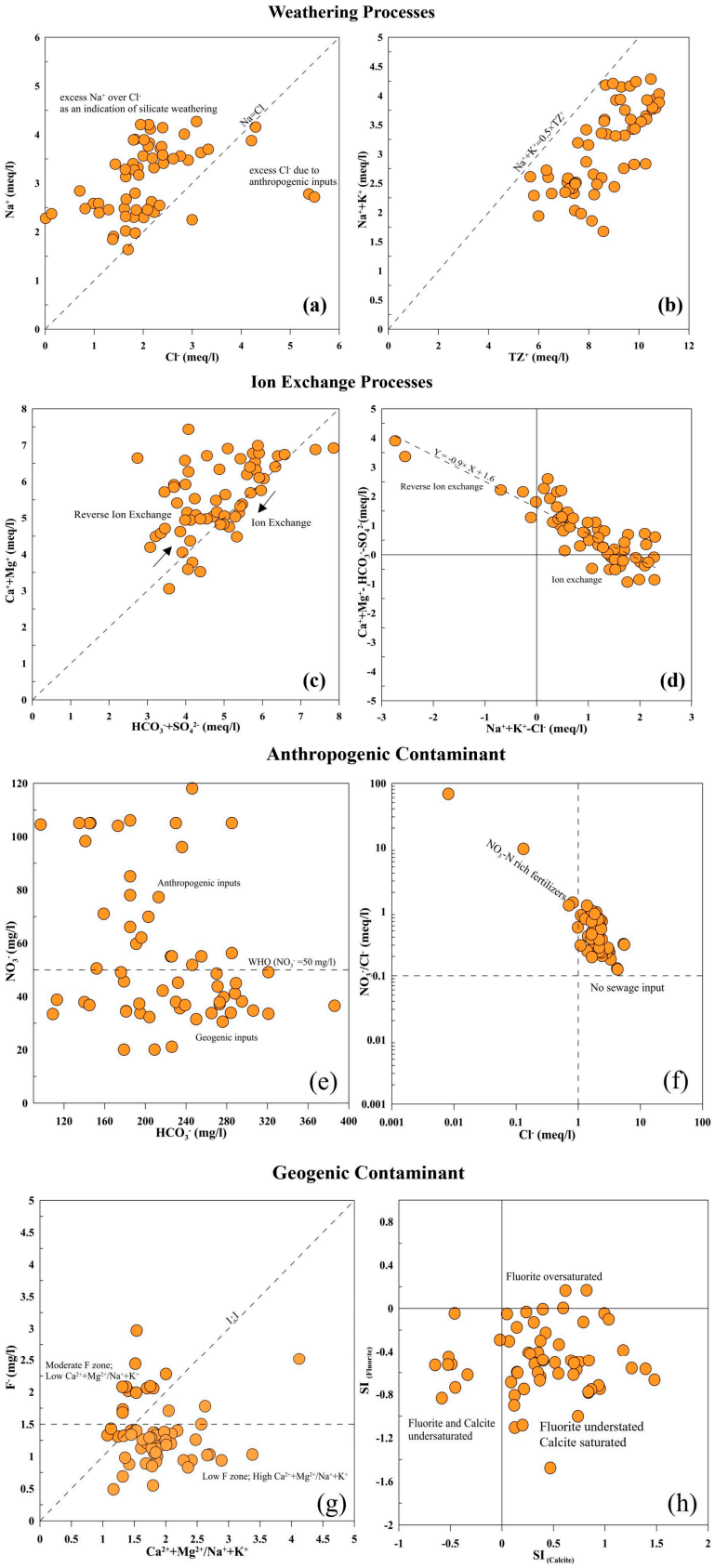


**Figure 7.** (**a**–**h**): Bivariate plots demonstrating the solute acquisition process: (**a**) $Na^+$ vs. $Cl^-$; (**b**) $TZ^+$ vs. $Na^+ + K^+$; (**c**) $SO_4^{2-} + HCO_3^-$ vs. $Mg^{2+} + Ca^{2+}$; (**d**) $Na^+ + K^+$-$Cl^-$ vs. $Ca^{2+} + Mg^{2+}$-$HCO^{3-}$-$SO_4^{2-}$; (**e**) $HCO_3^-$ vs. $NO_3^-$; (**f**) $Cl^-$ vs. $NO_3^-/Cl^-$; (**g**) $F^-$ vs. $Ca^{2+} + Mg^{2+}/Na^+ + K^+$; (**h**) the saturation index (calcite) vs. the saturation index (fluorite).

Groundwater samples falling below the 1:1 line in the bivariate plot of ($Ca^{2+}$ + $Mg^{2+}$) vs. ($HCO_3^-$ + $SO_4^{2-}$) indicate a contribution from sources of non-carbonate origin (Figure 7c), with the excess $HCO_3^-/SO_4^{2-}$ balanced by alkali cations ($Na^+$ + $K^+$). Similarly, samples falling above the equi-line show an excess of cations that would be balanced out by $Cl^-$ and other present anions. The molar ratio [($Ca^{2+}$ + $Mg^{2+}$)/$HCO_3^-$] value was found to be less than 1, whereas the unbalanced $HCO_3^-$ (left unbalanced by $Ca^{2+}$ + $Mg^{2+}$) is supposed to be balanced by $Na^+$ + $K^+$, which is derived from silicate weathering. The lithology showing carbonate dominance has a higher $Ca^{2+}/Na^+$ ratio, $Mg^{2+}/Na^+$ ratio, and HCO3-/Na+ ratio of 50, 10, and 120, respectively, but these ratios abruptly decrease in the silicate end members [67]. In the study area, $Ca^{2+}/Na^+$ = 1.16, $Mg^{2+}/Na^+$ = 0.73, and $HCO_3^-/Na^+$ = 1.14 show a high probability of silicate weathering. Few of the established thermodynamics-equilibrated equations responsible for the elevated concentration of these ions in the groundwater can be understood through Equations (13)–(15).

$$NaAlSi_3O_8 + 20H_2O + 2CO_2(g) \rightarrow Na^+ + 2HCO_3^- + 4H_4SiO_4 + Al_2Si_2O_5(OH)_4 \quad (13)$$

$$KAlSi_3O_8 + 20H_2O + 2CO_2(g) \rightarrow K^+ + 2HCO_3^- + 4H_4SiO_4 + Al_2Si_2O_5(OH)_4 \quad (14)$$

$$Ca_2\left(Mg,Fe\right)_4Al_2Si_7O_{22}\left(OH\right)_2 + 20H_2O + 2CO_2(g) \rightarrow 2Ca^{2+} + 4\left(Mg,Fe\right)^{2+} + 2HCO_3^- + 4H_4SiO_4 + Al_2Si_2O_5(OH)_4 \quad (15)$$

Ion exchange processes involve the interaction of groundwater with clay minerals, which involves either Na+ from the clay going into the groundwater or in a reverse ion exchange, with Na+ from groundwater replacing $Ca^{2+}$ and $Mg^{2+}$ from the aquifer matrix (Figure 7d). The present study area portrays the ion exchange reactions contributing metal cations to the groundwater. Furthermore, Figure 7d shows a negative alignment with a slope of −0.9, confirming the role of exchange reactions. The result also found that 43.3% of the groundwater samples exceeded the recommended value for nitrate (Table 1). Figure 7e displays the groundwater samples rich in $NO_3^-$ but usually low in $HCO_3^-$ concentration, which might be due to being recently recharged through irrigation return. Furthermore, Figure 7f depicts elevated contents of $NO_3^-/Cl^-$ in groundwater samples that have resulted from the use of nitrogen-based fertilizers contaminating the shallow groundwater at the local scale, although less prominent at the regional scale [11]. The F-rich groundwater is associated with low to moderate $Ca^{2+}$ + $Mg^{2+}/Na^+$ + $K^+$ under alkaline conditions (Figure 7g). The bivariate plot of the saturation index of calcite $SI_{calcite}$ vs. $SI_{fluorite}$ (Figure 7h) shows most of the groundwater samples falling in the fourth quadrant of the calcite-saturated and fluorite-undersaturated zone. This explains the removal of $Ca^{2+}$ through $CaCO_3$ precipitation and the further dissolution of $CaF_2$ (fluorite) that is present in the aquifer matrix through the following reaction (Equation (16)).

$$CaF_2 + 2HCO_3^- = CaCO_3 \text{ (precipitate)} + 2F^- + H_2O + CO_2 \quad (16)$$

### *3.3. Multivariate Statistical Approach*

#### 3.3.1. Factor Analysis

The factor analysis extracted five principal components with an eigenvalue > 1 for retention (Figure 8a), after varimax rotation with a total variance of 74% in the dataset (Table 2). The Kaiser–Meyer–Olkin sampling adequacy value for this study was 0.58, and Bartlett's test of sphericity test was < 0.05, which is well suited for the PCA. Factor 1 accounted for 32.3% of the total variance and was positively loaded with $Na^+$, $Ca^{2+}$, $HCO_3^-$, and EC, signifying the control of these ions in mineralization, and, for this region, this can be attributed to the geogenic factor. However, a few of the samples were also loaded with $NO_3^-$, derived through human-induced activities. Factor 2 contributed to 12.3% of the total variance and was in positive loading with $Cl^-$, $Ca^{2+}$, and $K^+$; a few groundwater samples were highly loaded with $NO_3^-$ concentration for this PC2 (Figure 8b). Factor 3 accounted for 11.5% of the variance, negatively loaded with pH and positively loaded with

$Ca^{2+}$ and $SO_4^{2-}$, while factors 4 and 5 accounted for 9.4% and 8.5% of the total variance, respectively. It has been noted that both geogenic and anthropogenic factors influence groundwater chemistry; however, based on the factor scores, geogenic causes seem to dominate in the present study area.

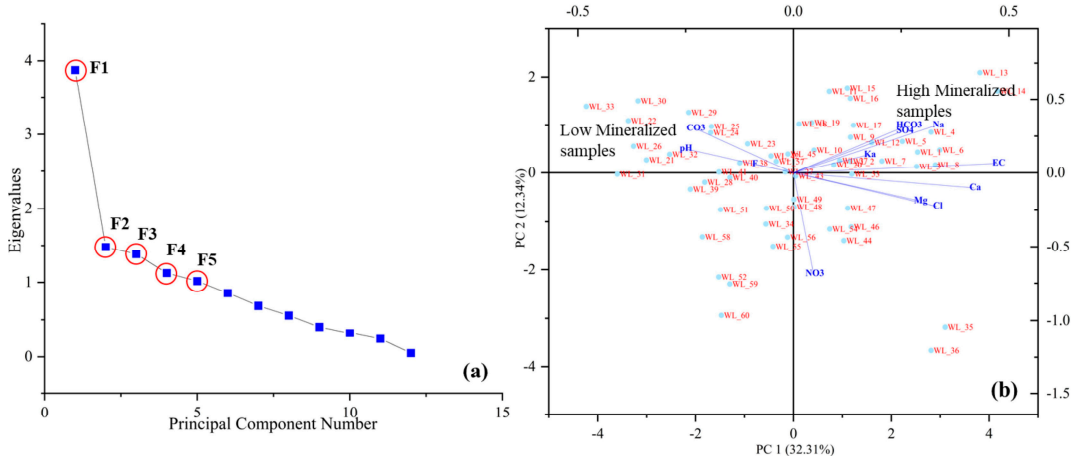


**Figure 8.** (**a**,**b**): Factor analysis results in (**a**) a scree plot with principal components (PCs) extracted for an eigenvalue greater than 1; (**b**) from the groundwater sample distribution in PC1 and PC2, it is evident that the groundwater samples falling in the right quadrant are comparatively more mineralized.

**Table 2.** Principal components (PCs) extracted through FA, with an eigenvalue of >1.

| Parameter | 1 | 2 | 3 | 4 | 5 |
|---|---|---|---|---|---|
| pH | 0.0 | −0.1 | −0.7 | 0.2 | 0.0 |
| EC (µS/cm) | 0.7 | 0.4 | 0.4 | −0.1 | 0.3 |
| $CO_3^{2-}$ | −0.4 | −0.3 | 0.0 | 0.6 | 0.2 |
| $HCO_3^-$ | 0.8 | −0.2 | 0.1 | 0.0 | 0.3 |
| $F^-$ | −0.1 | −0.1 | 0.2 | 0.0 | −0.7 |
| $Cl^-$ | 0.2 | 0.9 | 0.1 | −0.2 | 0.1 |
| $SO_4^{2-}$ | 0.2 | 0.0 | 0.8 | 0.3 | 0.0 |
| $NO_3^-$ | −0.2 | −0.1 | 0.1 | −0.8 | 0.3 |
| $Na^+$ | 0.8 | 0.3 | 0.1 | 0.1 | −0.1 |
| $Ka^+$ | 0.0 | 0.7 | 0.1 | 0.4 | 0.3 |
| $Mg^{2+}$ | 0.1 | 0.2 | 0.3 | −0.2 | 0.8 |
| $Ca^{2+}$ | 0.4 | 0.5 | 0.6 | −0.3 | 0.0 |
| % Variance | 32.3 | 12.3 | 11.5 | 9.4 | 8.5 |
| Cumulative % | 32.3 | 44.7 | 56.2 | 65.6 | 74.0 |

### 3.3.2. Hierarchical Cluster Analysis

Hierarchical clustering (HCA) was performed in both the row and column of the computed data matrix, and the data values were transferred to the color scale, which displays how the magnitude of the physicochemical parameters vary across each groundwater sample; HCA clustered them into two groups: cluster 1 and cluster 2. Since most of the variance in the dataset is attributed to Factors 1 and 2, which were then plotted with the samples to check the influence of these factors on the groundwater samples (Figure 8b), two clusters were retained for this study. Apart from these two samples (WL_35 and WL_36), the HCA result aligns with the result of the factor analysis (Figure 9). The row and column of the dendrogram correspond to physicochemical parameters and water samples, respectively. It is evident that the groundwater samples of cluster 1 are more mineralized concerning the $HCO_3^-$, $Mg^{2+}$, and $Na^+$ ions resulting from geogenic processes, as shown in the heatmap (Figure 9). However, a few of the groundwater samples also show the significant loading of $NO_3^-$, $Cl^-$, and $SO_4^{2-}$ for cluster 1, resulting from human-induced activities. In the field study, the samples of cluster 1 mostly fall in village/agricultural

lands that are affected by nitrate fertilizers. Cluster 2, on the other hand, is less mineralized compared to cluster 1, in terms of the major ions except $NO_3^-$ (Table 3; Figure 9). The sample locations of cluster 2 are further away from agricultural lands as they fall in or around townships, so these groundwater samples reflect lower nitrate contamination than those from cluster 1 locations. It is evident that most of the groundwater samples influenced by Factor 1 (Figure 8b) fall into cluster 1 (Figure 9). Thus, cluster 1 groundwater samples are comparatively more mineralized than those in cluster 2.

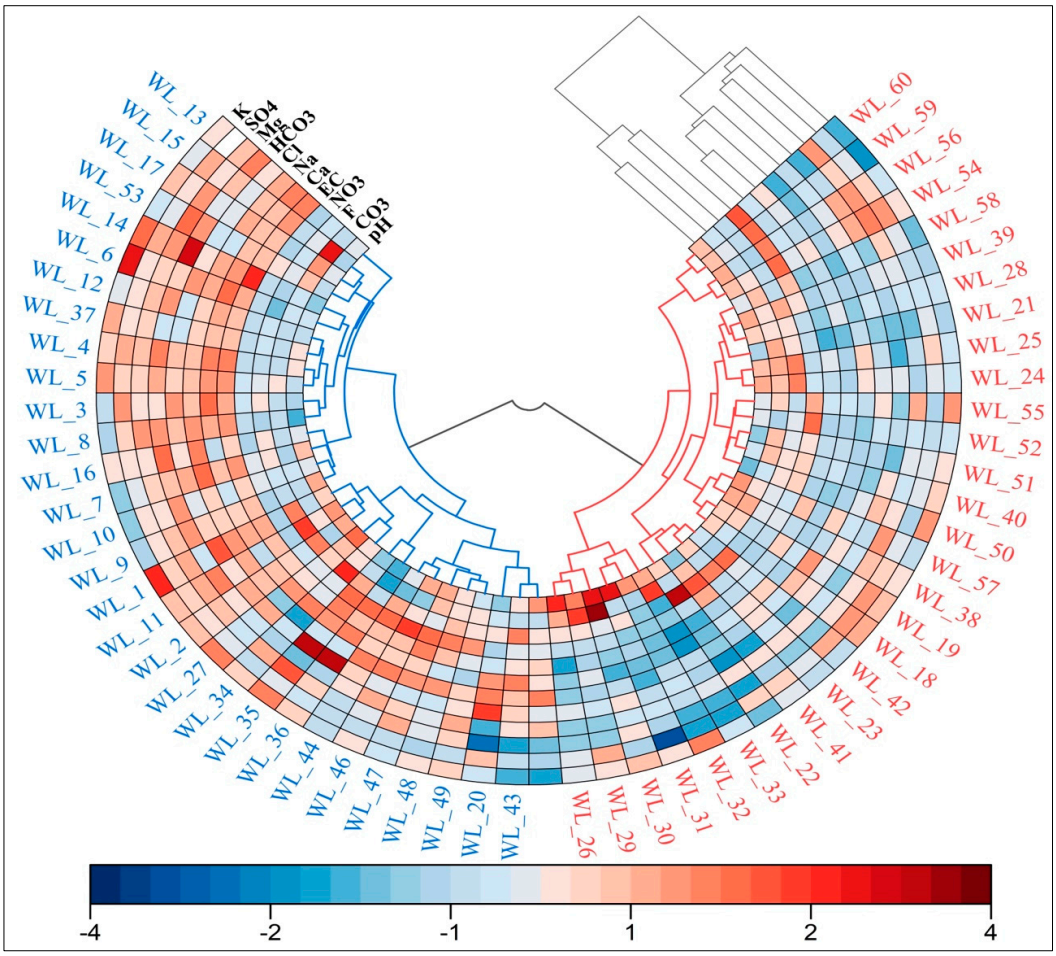


**Figure 9.** Dendrogram with a heatmap extracted using 12 physicochemical parameters; cluster 1 groundwater samples are more mineralized compared to the Cluster 2 groundwater samples.

**Table 3.** HCA resulted in two clusters, with their respective descriptive statistics.

| | Cluster 1 (n = 31) | | | | Cluster 2 (n = 29) | | | |
|---|---|---|---|---|---|---|---|---|
| **Parameter** | **Min** | **Max** | **Mean** | **Std Dev** | **Min** | **Max** | **Mean** | **Std Dev** |
| $CO_3^{2-}$ | 6.0 | 48.0 | 15.3 | 8.9 | 6.0 | 48.0 | 19.2 | 8.9 |
| $HCO_3^-$ | 97.0 | 386.0 | 249.2 | 60.8 | 113.0 | 289.0 | 187.2 | 38.2 |
| $F^-$ | 0.6 | 2.5 | 1.4 | 0.5 | 0.5 | 3.0 | 1.4 | 0.5 |
| $Cl^-$ | 60.0 | 195.0 | 94.3 | 35.1 | 0.3 | 82.9 | 54.8 | 21.1 |
| $SO_4^{2-}$ | 10.0 | 131.0 | 60.6 | 18.2 | 10.0 | 79.9 | 56.9 | 15.5 |
| $NO_3^-$ | 30.6 | 118.1 | 55.2 | 27.3 | 20.1 | 106.1 | 55.9 | 27.4 |
| $Na^+$ | 37.5 | 97.8 | 81.1 | 13.6 | 42.3 | 89.2 | 59.4 | 11.2 |
| $K^+$ | 0.1 | 2.8 | 1.3 | 0.6 | 0.0 | 2.0 | 1.1 | 0.5 |

**Table 3.** *Cont.*

| | Cluster 1 (n = 31) | | | | Cluster 2 (n = 29) | | | |
|---|---|---|---|---|---|---|---|---|
| **Parameter** | **Min** | **Max** | **Mean** | **Std Dev** | **Min** | **Max** | **Mean** | **Std Dev** |
| $Mg^{2+}$ | 5.3 | 40.2 | 27.9 | 7.4 | 11.1 | 36.4 | 23.2 | 7.3 |
| $Ca^{2+}$ | 56.1 | 89.9 | 76.5 | 8.6 | 41.1 | 72.6 | 59.4 | 7.4 |
| pH | 6.7 | 8.4 | 7.6 | 0.4 | 6.9 | 8.9 | 7.8 | 0.5 |
| TDS | 559.0 | 802.0 | 666.9 | 53.8 | 415.0 | 638.0 | 523.6 | 54.9 |
| EC (µS/cm) | 871.0 | 1247.0 | 1008.5 | 77.8 | 628.0 | 981.0 | 799.2 | 81.6 |

### *3.4. Spatial Distribution of $F^-$ and $NO_3^-$*

The concentrations of fluoride and nitrate have been spatially plotted, showing significant variations within the current study area. In the spatial interpolation process, the dissolved elemental concentrations of nitrate and fluoride were considered as random variables, and, using ordinary kriging, the data were transformed into a continuous surface. The thematic map shows the spatial distribution of fluoride, where the maximum and minimum concentrations in groundwater are 2.57 and 0.29, respectively, with an average value of 0.98 mg/L. The concentrations of fluoride in the various samples (~27%) exceed the permissible limits of the WHO, as has been identified in the Charkhari region. The alkaline nature of water is responsible for anionic exchanges, which may lead to the enhancement of fluoride concentrations in groundwater. The fluoride may be geogenic in origin, because of apatite weathering. The Bundelkhand gneissic complex has granitic rocks; the fluoride comes from the fluorapatite in granitic rocks and from the chemical dissolution of fluoride in groundwater by $CaF_2$. The hydroxide ion can replace the fluoride ion due to its negative charge and similarity in size. When the alkalinity of groundwater is high, hydroxyl ions readily replace the fluoride ions. About 70% of the total study area contains fluoride at its highest severity, which is in moderate concentrations (Figure 10a; Table 4). The Charkhari block has a relatively higher concentration of fluoride than other blocks like Panwari, Kabrai, and Jaitpur.

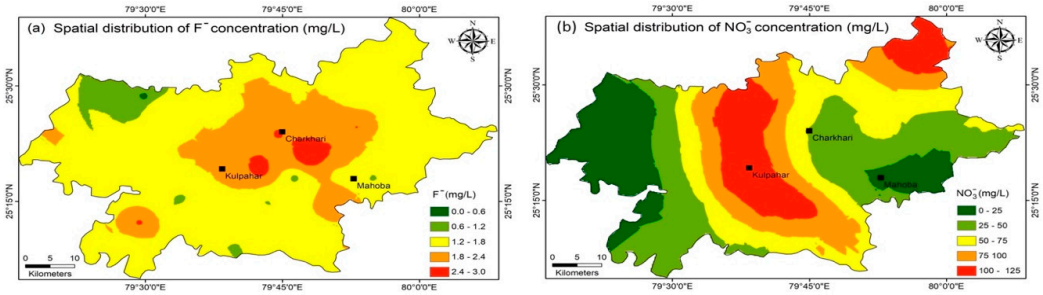


**Figure 10.** (**a**,**b**): Spatial distribution map of $F^-$ and $NO_3^-$ concentration derived using ordinary kriging.

**Table 4.** Spatial distribution of $F^-$ and $NO_3^-$ from ordinary kriging.

| **Index** | **Class** | **$F^-$** | | **Class** | **$NO_3^-$** | |
|---|---|---|---|---|---|---|
| | | **Area ($km^2$)** | **Area (%)** | | **Area ($km^2$)** | **Area (%)** |
| Very Low Concentration | 0–0.6 | 1.24 | 0.043 | 0–25 | 519.41 | 18.32 |
| Low Concentration | 0.6–1.2 | 161.86 | 5.613 | 25–50 | 793.07 | 27.97 |
| Moderate Concentration | 1.2–1.8 | 1992.71 | 69.092 | 50–75 | 629.98 | 22.22 |
| High Concentration | 1.8–2.4 | 648.25 | 22.48 | 75–100 | 471.35 | 16.63 |
| Very High Concentration | 2.4–3 | 79.94 | 2.772 | 100–125 | 421.22 | 14.86 |

The nitrate in groundwater primarily originates from agricultural fertilizers, with additional contributions from nearby waste, treatment plants, dairies, and domestic effluents. In the district, nitrate concentrations range from 20.08 to 118.09 mg/L, with an average of 55.57 mg/L. Spatially, higher concentrations are observed in the central region, following a north–south pattern, gradually decreasing towards the eastern and western boundaries (Figure 10b; Table 4). The Kulpahar and some parts of the Charkhari blocks are more affected by agricultural practices throughout the year. The fertilizer input is the major factor of nitrate contamination, but spatial maps of fluoride and nitrate are somehow oppositely correlated because fluoride is predominantly enhanced in an alkaline medium, whereas nitrate creates an acidic medium. However, the correlation cannot be established perfectly as fluoride is solely geogenically sourced, whereas nitrate is anthropogenically sourced, and their dominance primarily depends on the respective source concentration efficiency of contamination.

### *3.5. Semivariogram Models and the Predicted Probability Distribution of $F^-$ and $NO_3{}^-$*

As mentioned, of all the measured variables, the dissolved concentration of $F^-$ and $NO_3$ was found to be above the WHO 2017 permissible limit. The concentration of $F^-$ and $NO_3{}^-$ have been considered as random variables and were used to determine the predicted probability of risk-quantified estimates at unsampled locales using indicator kriging (IK). IK is a non-parametric approach that uses a structural component (spatial trend), spatially autocorrelated random variable (auto-correlation), and random noise (stochastic variation) for interpolation. The random variables ($F^-$ and $NO_3{}^-$) are transformed into indicator codes, and the spatial structure of the codes is best fitted to the experimental semivariogram model. The best-fit semivariogram model helps estimate the value of semivariogram parameters, i.e., nugget (Co), sill (C0 + C1), and range (C2, Lag distance), which later provides the value of semivariance ($\gamma_{(i)}$). Integrating the weights ($\lambda_i$) to the obtained semivariance value resulted in thematic maps depicting the spatial distribution of the projected probability of $NO_3$ and F. The predicted probability of $F^-$ and $NO_3{}^-$, as determined from the semivariogram model, shows variable classes ranging between 0 and 1.

The best-fitting experimental semivariogram model for $F^-$ and $NO_3{}^-$ is exponential and indicates the nugget (C0) variance as 0. The zero-nugget variance suggests that the random variables ($F^-$ and $NO_3{}^-$) that have been transformed to the indicator codes are significantly spatially auto-correlated within the range (C2) of 27.65 and 56.22 km, respectively (Figure 11a,b; Table 5). In addition, a small nugget value also suggests that the indicator kriging method chosen to determine the predicted probability of the random variable performs well. However, the range variation (the lag distance upon which spatially autocorrelated indicator codes are present) given by the exponential semivariogram models of $F^-$ and $NO_3{}^-$ indicate various sources of $F^-$ and $NO_3{}^-$. The maximum value of the semivariance, i.e., the sill (C0 + C1), for a semivariogram model of $F^-$ and $NO_3{}^-$ are 24.58 and 20.74, respectively, which values are relatively higher than the nugget variance (Figure 11a,b; Table 5). The exponential semivariogram successfully models the random variables defined by the indicator codes, with no anisotropy seen. The prediction error and cross-validation for IK were achieved through the predicted mean error (PMR), root mean square predicted standardized error (RMS-PSE), root mean square error (RMS), and average standard error (ASE) (Figure 12a,b and Table 6). The predicted probability of $F^-$ and $NO_3{}^-$, as determined from IK, have been classified into 0.0–0.2 (very low), 0.2–0.4 (low), 0.4–0.6 (moderate), 0.6–0.8 (high), and 0.8–1.0 (very high), based on their predicted concentration spatial distribution (Figure 13a,b) and (Table 7). The results indicated that most of the areas around Kulpahad and Charkhari, covering ~14–16% of central Mahoba district, fall within the high to very high probability class. The areas occupied by the high to very high probability classes of $F^-$ and $NO_3{}^-$ mostly fall within the rural sector and have negligible human populations, suggesting that the high predicted probability of $NO_3{}^-$ can be exclusively attributed to the use of fertilizers on farms. The regional groundwater flow in the study area could be the cause of the probability distribution's steady reduction

from the southwest to the northeast directions. As discussed earlier, nitrate concentration decreases gradually from the central to the eastern and western ends of the district.

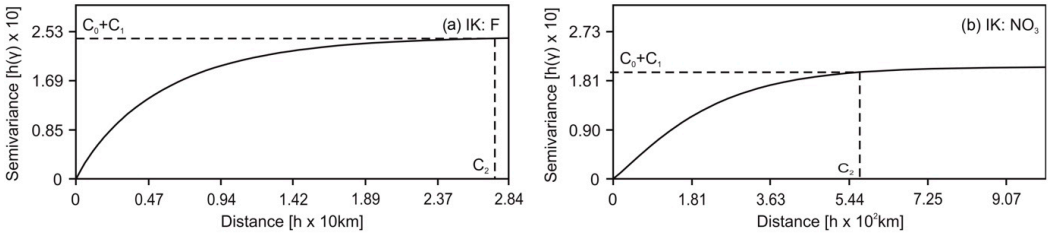


**Figure 11.** (**a**,**b**): Best-fitted experiential semivariogram plot $F^-$ and $NO_3^-$ concentration.

**Table 5.** Semivariogram parameters (nugget, sill, and range) derived from the best-fitting theoretical model.

| Method | Transformed Variables | Semivariogram Model | Threshold | Semivariogram Parameters | | | Anisotropy |
|---|---|---|---|---|---|---|---|
| | | | | Nugget ($C_0$) | Sill ($C_0 + C_1$) | Range ($C_2$) | |
| IK | F | Exponential | 1.5 | 0 | 24.58 | 27.65 | No |
| IK | $NO_3$ | Exponential | 50 | 0 | 20.74 | 56.22 | No |

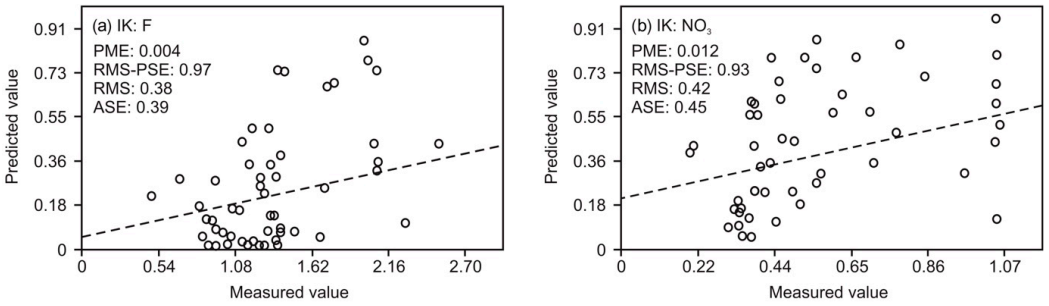


**Figure 12.** (**a**,**b**): Cross-validation plots for IK showing the relationship between the measured and predicted indicator values of $F^-$ and $NO_3^-$ concentration.

**Table 6.** Prediction error and cross-validation results for IK.

| Method | Transformed Variables | Semivariogram Model | Predicted Mean Error (PME) | Root Mean Square Predicted Standardized Error (RMS-PSE) | Root Mean Square Error (RMS) | Average Standard Error (ASE) |
|---|---|---|---|---|---|---|
| IK | F | Exponential | 0.004 | 0.97 | 0.38 | 0.39 |
| IK | $NO_3$ | Exponential | 0.012 | 0.93 | 0.42 | 0.45 |

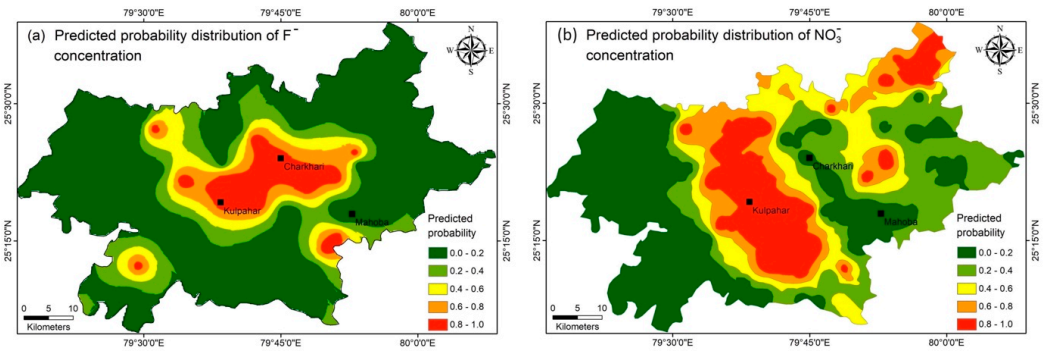


**Figure 13.** (**a**,**b**): Predicted probability distribution maps of $F^-$ and $NO_3^-$ concentrations in drinking groundwater using indicator kriging.

**Table 7.** Predicted probability distribution of $F^-$ and $NO_3^-$ from IK.

| Index | Class | $F^-$ | | $NO_3^-$ | |
|---|---|---|---|---|---|
| | | Area ($km^2$) | Area (%) | Area ($km^2$) | Area (%) |
| Very Low Probability | 0–0.2 | 1811.38 | 63.89 | 1047.62 | 36.95 |
| Low Probability | 0.2–0.4 | 405.35 | 14.30 | 604.09 | 21.31 |
| Moderate Probability | 0.4–0.6 | 238.08 | 8.40 | 426.02 | 15.03 |
| High Probability | 0.6–0.8 | 184.7 | 6.51 | 304.38 | 10.74 |
| Very High Probability | 0.8–1.0 | 195.52 | 6.90 | 452.92 | 15.98 |

### *3.6. Health Risks from Exposure to $F^-$ and $NO_3^-$*

The hazard index (HI) denotes the sum fraction of the non-carcinogenic contaminants measured in drinking water and is used to estimate the risk of health effects [30,68]. Without any means of water treatment, people living in rural India are compelled to consume contaminated groundwater for potable use. HI from exposure to combined $F^-$ and $NO_3^-$ in drinking water can be calculated using the USEPA approach. This approach is empirical and combines standard body mass and exposure time, as used in the present study. The USEPA recommends estimating the health risks individually for males, females, and infants [69]. However, as no record of demographic data is available for the study area, the urbanization index (UI) derived from the human population data from the CIESIN and DSMP night-time light data has been used to estimate the human health risk from exposure to $F^-$ and $NO_3^-$ in the drinking water (Figure 14).

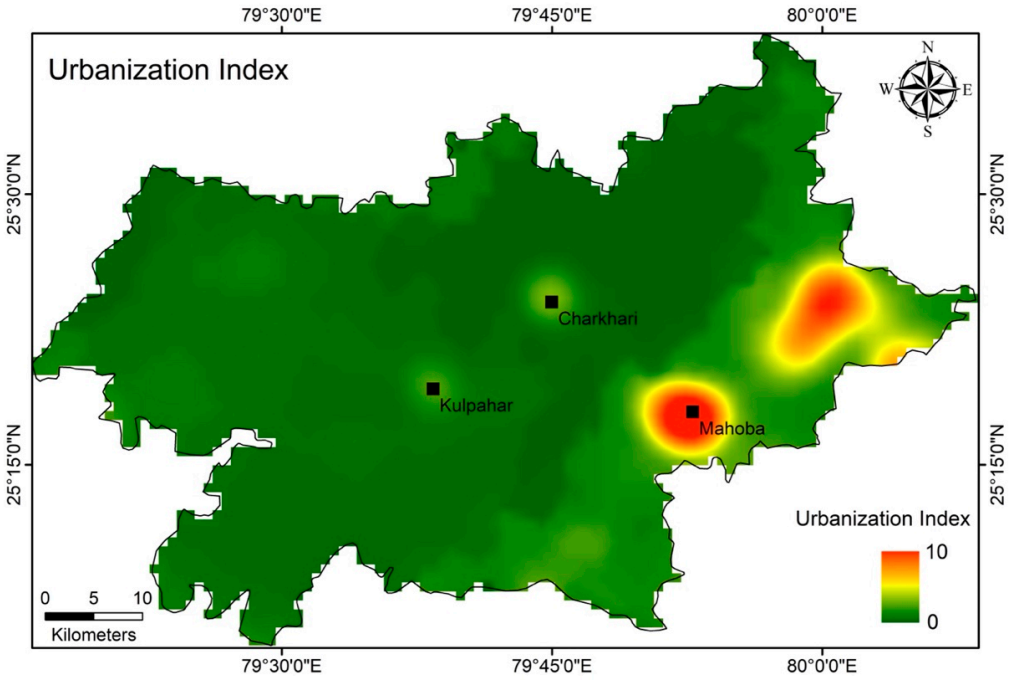


**Figure 14.** Urbanization index (UI) derived from the integration of DMSP-OLS, VIIRS, and the gridded population density dataset from CIESIN.

The derived HI (Figure 15a) indicates the spatial distribution of risk due to the consumption of $F^-$ and $NO_3^-$-contaminated water. The HI is classified into five classes, from very low to very high. The health risk is potentially alarming in the central parts around Kulpahar and Charkhari, indicating that ~23% of the total area is above high health risk (Figure 13; Table 8). The human health risk index classes correspond to the geographic distribution of the probability of threats to human health. The regional distribution of the HI, as predicted by Equation (10), has been associated with the urbanization index (UI), yielding a composite health risk map (Figure 15b). The health risk map calculates

the impacted area and the urban population affected due to contamination by $F^-$ and $NO_3^-$ ions exceeding acceptable levels. The high fluoride and nitrate levels in groundwater have a deleterious influence on human health. The human health risk map shows the distribution of health risks to the human population from exposure to a prolonged intake of water contaminated with $F^-$ and $NO_3^-$. The derived human health risk map has been classified into five classes from 0–15, representing very low to very high health risks, respectively (Figure 15b; Table 9). The results indicated that the areas lying towards the east and southeast show a high risk to human health from exposure to contaminated drinking water. Since HHRI is closely linked with the spatial distribution of urbanization (high population density in the east and southeast), the health risk from exposure to contaminated drinking water is also high in the east and southeast of the study area. The gradual decrease in the health risk from the south and southeast to the west is due to the negligible population density in most of the populated area.

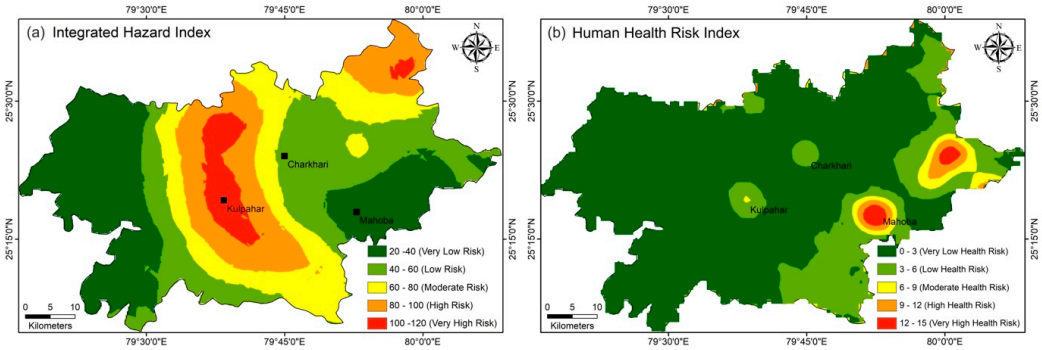


**Figure 15.** (**a**) The hazard index of $F^-$ and $NO_3^-$; (**b**) the human health risk index, showing the spatial extent of varying degrees of risk due to $F^-$ and $NO_3^-$ concentrations in the groundwater. Note that the extent of high to very high health risk lies around the urban center of Mahoba.

**Table 8.** Integrated hazard index (HI), derived from the USEPA 2012 approach.

| Class | Index | Area ($km^2$) | Area (%) |
|---|---|---|---|
| 20–40 | Very Low Risk | 897.24 | 31.65 |
| 40–60 | Low Risk | 698.34 | 24.63 |
| 60–80 | Moderate Risk | 594.45 | 20.97 |
| 80–100 | High Risk | 486.18 | 17.15 |
| 100–120 | Very High Risk | 158.82 | 5.60 |

**Table 9.** Human health risk index (HHRI) distribution from exposure to $F^-$ and $NO_3^-$.

| Class | Risk Index | Index | Area ($km^2$) | Area (%) |
|---|---|---|---|---|
| 0–3 | I | Very Low Health Risk | 2168.43 | 76.49 |
| 3–6 | II | Low Health Risk | 523.10 | 18.45 |
| 6–9 | III | Moderate Health Risk | 74.65 | 2.63 |
| 9–12 | IV | High Heath Risk | 44.32 | 1.56 |
| 12–15 | V | Very High Health Risk | 24.51 | 0.86 |

The findings of this study have significant implications for regions facing similar groundwater contamination challenges. Across India, especially in other parts of the Indo-Gangetic Plain and peninsular regions, geogenic fluoride contamination and nitrate pollution from agricultural runoff are pervasive (Kumar and Singh, 2022). Globally, rural areas in arid and semi-arid zones, such as in Sub-Saharan Africa, parts of China, and Latin America, also encounter groundwater contamination due to analogous geogenic and anthropogenic factors [14,30]. This study's integrated approach, employing geospatial, statistical, and health risk assessment techniques, provides a replicable framework for

identifying contamination hotspots and prioritizing areas for intervention. Policymakers and water resource managers can leverage this methodology to design targeted mitigation strategies, fostering sustainable groundwater use and public health safeguards worldwide.

## 4. Limitations and Constraints

The Mahoba district, representing the present study area, is characterized by gently sloping terrain predominantly composed of granite, granodiorite, granitic gneisses, and dolerite, due to its location within the Bundelkhand Massif Terrain. Consequently, the study area primarily comprises impermeable hard rock formations, where groundwater occurs mainly through fracture filling (secondary porosity), making it widely distributed across the region [70]. Given the hard rock-dominated nature of the region, the groundwater sampling strategy for this study was carefully designed, based on (a) the accessibility of the region, (b) groundwater usage by the locals, and (c) avoiding oversampling and ensuring maximum geological heterogeneity.

One of the primary objectives of this study was to identify the controlling factors influencing groundwater chemistry and its spatial variability, using multivariate statistical approaches and geostatistical modeling. Therefore, the samples were collected in a stratified random sampling manner to minimize the uncertainty in the space. Thus, the total number of samples collected ($n$ = 60) through the random sample collection method not only covered the maximum area (geology), as outlined in Figure 1 of this manuscript, but was also uniformly distributed, making it an excellent choice for any interpolation techniques to be adopted. Also, since the area has uniform aquifer conditions (as represented by rocky aquifers in a granitic complex), the groundwater geochemistry in the study area is the same throughout the subsurface region at different levels. This strengthens the idea of applying the interpolation technique for use at a larger spatial extent.

For any interpolation method, the number of samples to be collected and their distribution in space are critical, as this controls the accuracy of the measurement. In the present approach, the number of samples ($n$ = 60) collected was subject to the availability of India Mark-II hand pumps. However, we made sure that all the samples were collected in a stratified random sampling method and so should have a uniform distribution (i.e., they were collected from all parts of the study area), which was a prerequisite of any interpolation method to be performed.

Each sample was analyzed for fluoride ($F^-$) and nitrate ($NO_3{}^-$), which were later considered random variables. To transform these random variables into a continuous raster surface (spatial distribution), a technique called "Kriging", which is a statistically based "optimal" estimator of spatial variables, was adopted. Kriging uses regionalized variable theory to explain the autocorrelation between random variables through a semivariogram function. The best interpolation method depends on the character and assumptions of data behavior. Therefore, in the present approach, several methods have been explored and selected, based on semivariogram parameters and cross-validation estimates for different kriging methods, showing the relationship between the measured and predicted indicator values of $F^-$ and $NO_3{}^-$ concentrations. The optimal interpolator (indicator kriging (IK); a co-kriging approach is found most applicable in the present case) was chosen, based on a semivariogram parameter called "nugget" that indicates an initial semivariance when autocorrelation is highest (intercept), or just no uncertainty where the distance is close to 0 ($\varepsilon$"). The best fit of experimental semivariogram model for $F^-$ and $NO_3{}^-$) was exponential and indicated a nugget variance of 0 (Figure 11a,b; Table 5). In addition, IK was used to measure the uncertainty or random noise representing stochastic variation independent of sample location. IK allowed the probability-based prediction of $F^-$ and $NO_3{}^-$) by transforming them into binary indicator codes, based on thresholds.

## 5. Conclusions and Ways Forward

The area of the study region, characterized by a semi-arid climate and a gneissic-granitic geological complex, faces critical groundwater quality and quantity challenges.

Groundwater depletion exacerbates strong rock–water interactions, leading to higher concentrations of solutes such as fluoride and contributing to the deterioration of water quality. Detailed hydrogeochemical analysis showed that the primary water types are Na-$HCO_3$, Ca-$HCO_3$, Ca-Mg-$HCO_3$, and Ca-Na-$HCO_3$. These chemical signatures suggest that processes such as silicate weathering and reverse ion exchange mainly drive geogenic contamination. Agriculture dominates the regional economy, but the thin alluvium cover limits productivity, prompting the frequent usage of chemical fertilizers. This practice directly contributes to elevated nitrate contamination in the groundwater. Statistical analysis through factor analysis extracted five principal components of contamination sources: (1) geogenic mineralization (32.3% of the total variance), (2) anthropogenic sources (12.3%), and (3–5) mixed sources. Hierarchical cluster analysis (HCA) corroborated these findings, linking the high nitrate levels in cluster 1 to agricultural activities, while cluster 2, located away from farmland, exhibited lower contamination. Notably, 30% of the samples had high fluoride levels beyond the WHO-permitted limits. A human health risk assessment was conducted to evaluate non-carcinogenic risks, using the hazard quotient of fluoride and nitrate exposure through drinking water. The urban populations exhibited the highest risk probability, due to higher groundwater reliance and population density. However, the current risk assessment lacked a comprehensive analysis of demographic variables such as age, sex, and rural–urban differences, which could provide a more detailed understanding of the health impacts. Based on the above findings, the following mitigation strategies have been proposed:

1. Implementing rooftop rainwater harvesting and recharge wells can dilute fluoride concentrations, lowering them to permissible levels.
2. Affordable government-subsidized methods can help to mitigate fluoride and nitrate contamination effectively.
3. Promoting hybrid crops, precision irrigation (e.g., sprinklers), and optimal groundwater use can reduce nitrate runoff and preserve groundwater quality.
4. Raising awareness about water quality and conservation can encourage better practices and informed decision-making.

By integrating geospatial and statistical approaches with sustainable practices, these measures aim to address groundwater contamination and ensure long-term water security in the studied region and can be implemented on a national scale.

**Supplementary Materials:** The following supporting information can be downloaded at: https://www.mdpi.com/article/10.3390/w16243683/s1, Table S1: Detailed geochemical analysis of the groundwater samples (n = 60).

**Author Contributions:** Conceptualization, D.S.G. and A.R.; methodology, D.S.G., A.P. and A.R.; software, D.S.G., A.P. and A.R.; validation, A.K. (Amit Kumar) and S.K.C.; formal analysis, D.S.G. and A.R.; investigation, A.K. (Amit Kumar), V.S. and A.K. (Ankit Kumar); data curation, D.S.G., A.P. and A.R.; writing—original draft, D.S.G., A.P. and A.R.; writing—review and editing, D.S.G., A.P., A.R., V.S., S.K.C., A.K. (Ankit Kumar), R.K. and S.S.R.; funding acquisition, A.K. (Amit Kumar). All authors have read and agreed to the published version of the manuscript.

**Funding:** This research received no external funding.

**Data Availability Statement:** Data used in this study are available on reasonable request from the corresponding author.

**Acknowledgments:** The authors acknowledge the Institute of Eminence (IoE), Banaras Hindu University (BHU), Defence Geoinformatics Research Establishment (DGRE), and Central Instrument Facility, Indian Institute of Technology—BHU for extending their support to conduct this work.

**Conflicts of Interest:** The authors declare no conflicts of interest.

## References


1. Sen Gupta, D.; Ghosh, P.; Rai, S.P.; Tripathi, S. Hydrogeochemical variability and appraisal of water quality of groundwater in Mahoba district, Uttar Pradesh, India. *Environ. Earth Sci.* **2022**, *81*, 149. [CrossRef]
2. Kumar, S.; Singh, A. Geospatial analysis of groundwater contamination in semi-arid regions: A case study from India. *Environ. Monit. Assess.* **2022**, *194*, 567.
3. Shyam, R.; Krishan, G.; Kheraj Kumar, A. Evaluation of groundwater quality for life-supporting activities: A case study of Haryana, India. *Int. J. River Basin Manag.* **2024**, *22*, 297–308. [CrossRef]
4. Singh, A.; Raju, A.; Kumar, S.; Chandniha, S.K.; Singh, L.; Tyagi, I.; Karri, R.R.; Kumar, A. Hydrogeochemical characterization of groundwater and their associated potential health risks. *Environ. Sci. Pollut. Res.* **2022**, *30*, 14993–15008. [CrossRef]
5. Kimambo, V.; Bhattacharya, P.; Mtalo, F.; Ahmad, A. Fluoride occurrence in groundwater systems at global scale and status of defluoridation-State of the art. *Groundw. Sustain. Dev.* **2019**, *9*, 100223. [CrossRef]
6. Raju, A.; Singh, R.P.; Kannojiya, P.K.; Patel, A.; Singh, S.; Sinha, M. Declining groundwater and its impacts along Ganga riverfronts using combined Sentinel-1, GRACE, water levels, and rainfall data. *Sci. Total Environ.* **2024**, *920*, 170932. [CrossRef]
7. Shaji, E.; Sarath, K.V.; Santosh, M.; Krishnaprasad, P.K.; Arya, B.K.; Babu, S.B. Fluoride contamination in groundwater: A global review of the status, processes, challenges, and remedial measures. *Geosci. Front.* **2024**, *15*, 101734. [CrossRef]
8. Singh, G.; Kumari, B.; Sinam, G.; Kriti Kumar, N.; Mallick, S. Fluoride distribution and contamination in the water, soil and plants continuum and its remedial technologies, an Indian perspective– a review. *Environ. Pollut.* **2018**, *239*, 95–108. [CrossRef] [PubMed]
9. Patel, A.; Rai, S.P.; Akpataku, K.V.; Puthiyottil, N.; Singh, A.K.; Pant, N.; Noble, J. Hydrogeochemical characterization of groundwater in the shallow aquifer system of Middle Ganga Basin, India. *Groundw. Sustain. Dev.* **2023**, *21*, 100934. [CrossRef]
10. Patel, A.; Rai, S.P.; Puthiyottil, N.; Singh, A.K.; Noble, J.; Singh, R.; Hagare, D.; Kumar, U.S.; Rai, N.; Akpataku, K.V. Refining aquifer heterogeneity and understanding groundwater recharge sources in an intensively exploited agrarian dominated region of the Ganga Plain. *Geosci. Front.* **2024**, *15*, 101808. [CrossRef]
11. Patel, A.; Singh, A.K.; Singh, R.; Puthiyottil, N.; Rai, S.P. Fluoride Mobilization and Provenance Identification in Semi-arid Conditions: A Hydrochemical and Isotopic Approach. In *Surface and Groundwater Resources Development and Management in Semi-arid Region: Strategies and Solutions for Sustainable Water Management*; Springer International Publishing: Cham, Switzerland, 2023; pp. 97–116.
12. Ali, S.A.; Ali, U. Hydrochemical characteristics and spatial analysis of groundwater quality in parts of Bundelkhand massif. India. *Appl. Water Sci.* **2018**, *8*, 39. [CrossRef]
13. Arslan, H. Spatial and Temporal Mapping of Groundwater Salinity Using Ordinary Kriging and Indicator Kriging: The Case of Bafra Plain, Turkey. *Agric. Water Manag.* **2012**, *113*, 57–63. [CrossRef]
14. Zhang, W.; Wang, S.; Huang, H. Assessment of groundwater quality and health risks in nitrate-affected regions: Insights from a case study in northern China. *Sci. Total Environ.* **2020**, *740*, 140087.
15. Ahmad, S.; Singh, R.; Arfin, T.; Neeti, K. Fluoride contamination, consequences and removal techniques in water: A review. *Environ. Sci. Adv.* **2022**, *1*, 620–661. [CrossRef]
16. Khan, M.Y.A.; El Kashouty, M.; Gusti, W.; Kumar, A.; Subyani, A.M.; Alshehri, A. Geo-Temporal Signatures of Physicochemical and Heavy Metals Pollution in Groundwater of Khulais Region—Makkah Province, Saudi Arabia. *Front. Environ. Sci.* **2022**, *9*, 800517. [CrossRef]
17. Krishan, G.; Rao, M.S.; Vashisht, R.; Chaudhary, A.; Singh, J.; Kumar, A. Isotopic Assessment of Groundwater Salinity: A Case Study of the Southwest (SW) Region of Punjab, India. *Water* **2022**, *14*, 133. [CrossRef]
18. Laxman Kumar, D. Health risk assessment of nitrate and fluoride toxicity in groundwater contamination in the semi-arid area of Medchal, South India. *Appl. Water Sci.* **2022**, *12*, 11.
19. Li, C.; Gao, X.; Wang, Y. Hydrogeochemistry of high-fluoride groundwater at Yuncheng Basin, northern China. *Sci. Total Environ.* **2015**, *508*, 155–165. [CrossRef] [PubMed]
20. Mankikar, T.Y. Geological controls on fluoride contamination of unconfined aquifer in Mahoba district. *Arab. J. Geosci.* **2022**, *15*, 978. [CrossRef]
21. Raju, A.; Singh, A. Assessment of groundwater quality and mapping human health risk in central Ganga alluvial plain, Northern India. *Environ. Process.* **2017**, *4*, 375–397. [CrossRef]
22. Raju, A.; Singh, A.; Srivastava, N.; Singh, S.; Jigyasu, D.K.; Singh, M. Mapping Human Health Risk by Geostatistical Method: A Case Study of Mercury in Drinking Groundwater Resource of the Central Ganga Alluvial Plain, Northern India. *Environ. Monit. Assess.* **2019**, *191* (Suppl. S2), 298. [CrossRef]
23. Raju, N.J.; Ram, P.; Dey, S. Groundwater quality in the lower Varuna River basin, Varanasi district, Uttar Pradesh, India. *J. Geol. Soc. India* **2009**, *73*, 178–192. [CrossRef]
24. Raju, A.; Singh, A.; Chandniha, S.K. A synergetic approach for quantification and analysis of coal fires in Jharia Coalfield, India. *Phys. Chem. Earth* **2023**, *131*, 103441. [CrossRef]
25. Rawat, U.; Awasthi, A.; Gupta, D.S.; Paul, R.S.; Tripathi, S. Morphometric analysis using remote sensing and GIS techniques in the Bagain river basin, Bundelkhand region, India. *Indian J. Sci. Technol.* **2017**. [CrossRef]
26. Skold, A.; Cosco, D.L.; Klein, R. (2011) Methemoglobinemia: Pathogenesis, Diagnosis, and Management. *South. Med. J.* **2011**, *104*, 757–761. [CrossRef] [PubMed]

27. Toolabi, A.; Bonyadi, Z.; Paydar, M.; Najafpoor, A.A.; Ramavandi, B. Spatial distribution, occurrence, and health risk assessment of nitrate, Fluoride, and arsenic in Bam groundwater resource, Iran. *Groundw. Sustain. Dev.* **2021**, *12*, 100543. [CrossRef]
28. Vikas, D.; Sharma, S. Fluoride contamination in drinking water and associated health risk assessment in the Malwa Belt of Punjab, India. *Environ. Adv.* **2022**, *8*, 100242.
29. Abascal, E.; Gómez-Coma, L.; Ortiz, I.; Ortiz, A. Global diagnosis of nitrate pollution in groundwater and review of removal technologies. *Sci. Total Environ.* **2022**, *810*, 152233. [CrossRef]
30. USEPA. *Human Health Risk Assessment*; United States Environmental Protection Agency: Washington, DC, USA, 2019.
31. Dwivedi, L.; Gupta, D.S.; Tripathi, S. Groundwater potential mapping of Ukmeh river watershed area of Upper Vindhyan region using remote sensing and GIS. *Indian J. Sci. Technol.* **2016**, *9*, 1–7. [CrossRef]
32. Handa, B.K. Geochemistry and genesis of Fluoride containing ground waters in India. *Groundwater* **1975**, *13*, 275–281. [CrossRef]
33. Mukherjee, A.; Fryar, A.E. Deeper groundwater chemistry and geochemical modeling of the arsenic affected western Bengal basin, West Bengal, India. *Appl. Geochem.* **2008**, *23*, 863–894. [CrossRef]
34. Narsimha, A.; Li, P.; Qian, H. Evaluation of groundwater contamination for Fluoride and nitrate in semi-arid region of Nirmal Province, South India: A special emphasis on human health risk assessment (HHRA). *Hum. Ecol. Risk Assess. Int. J.* **2018**, *25*, 1107–1124.
35. Pandey, H.K.; Singh, V.K.; Singh, S.K. Multi-criteria decision making and Dempster-Shafer model–based delineation of groundwater prospect zones from a semi-arid environment. *Environ. Sci. Pollut. Res.* **2022**, *29*, 47740–47758. [CrossRef] [PubMed]
36. Paul, R.S.; Rawat, U.; Gupta, D.S.; Biswas, A.; Tripathi, S.; Ghosh, P. Assessment of groundwater potential zones using multi-criteria evaluation technique of Paisuni river Basin from the combined state of Uttar Pradesh and Madhya Pradesh, India. *Environ. Earth Sci.* **2020**, *7*, 340. [CrossRef]
37. Rose, S. Comparative major ion geochemistry of piedmont streams in the Atlanta, Georgia region: Possible efects of urbanization. *Environ. Geol.* **2002**, *42*, 102–113. [CrossRef]
38. Bajpai, R.; Shukla, V.; Raju, A.; Singh, C.P.; Upreti, D.K. A geostatistical approach to compare metal accumulation pattern by lichens in plain and mountainous regions of northern and central India. *Environ. Earth Sci.* **2022**, *81*, 203. [CrossRef]
39. Bhowmik, A.K.; Alamdar, A.; Katsoyiannis, I.; Shen, H.; Ali, N.; Ali, S.M.; Bokhari, H.; Schafer, R.B.; Eqani, S.A.M.A.S. Mapping human health risks from exposure to trace metal contamination of drinking water sources in Pakistan. *Sci. Total Environ.* **2015**, *538*, 306–316. [CrossRef]
40. Abhay, K.S.; Raj, B.; Tiwari, A.K.; Mahato, M.K. Evaluation of hydrogeochemical processes and groundwater quality in the Jhansi district of Bundelkhand region, India. *Environ. Earth Sci.* **2012**, *70*, 1225–1247. [CrossRef]
41. Adhikary, P.P.; Dash, C.; Bej, R.; Chandrasekharan, H. Indicator and Probability Kriging Methods for Delineating Cu, Fe, and Mn Contamination in Groundwater of Najafgarh Block, Delhi, India. *Environ. Monit. Assess.* **2011**, *176*, 663–676. [CrossRef]
42. Adimalla, N.; Rajitha, S. Spatial distribution and seasonal variation in fluoride enrichment in groundwater and its associated human health risk assessment in Telangana State, South India. *Hum. Ecol. Risk Assess. Int. J.* **2018**, *24*, 2119–2132.
43. Gupta, D.S.; Tripathi, S.; Ghosh, P. A Quantitative Morphometric Analysis of Barhar River Watershed of Mahoba district, U.P.; India using Remote Sensing and GIS. *Indian J. Sci. Technol.* **2017**, *10*, 1–5. [CrossRef]
44. Hounslow, A.W. *Water Quality Data: Analysis and Interpretation*; CRC Lewis Publishers: New York, NY, USA, 1995.
45. Jabrinder, S.; Bhardwaj, P.; Abhishek, A. Health implications among school children due to Fluoride in underground aquifers of Haryana state, India. *Environ. Qual. Manag.* **2022**, *31*, 233–240.
46. Sajil Kumar, P.J. Hydrogeochemical and multivariate statistical appraisal of pollution sources in the groundwater of the lower Bhavani River basin in Tamil Nadu. *Geol. Ecol. Landsc.* **2020**, *4*, 40–51. [CrossRef]
47. Sarin, M.M.; Krishnaswami, S.; Dilli, S.B.L.K.; Moore, W.S. Major ion chemistry the Ganga-Brahmaputra River system: Weathering processes and fuxes of the Bengal. *Geochem. Cosmochim Acta* **1989**, *53*, 997–1009. [CrossRef]
48. Karunanidhi, D.; Aravinthasamy, P.; Subramani, T.; Roy, P.D.; Srinivasamoorthy, K. Risk of fluoride-rich groundwater on human health: Remediation through managed aquifer recharge in a hard rock terrain South India. *Nat. Resour. Res.* **2020**, *29*, 2369–2395. [CrossRef]
49. Devi, V.; Atique, M.M.; Raju, A.; Upreti, G.; Jigyasu, D.K.; Yadav, J.K.; Singh, S.; Kar, R.; Singh, M. Mercury transportation dynamics in the Ganga Alluvial Plain, India: Rainwater-groundwater-river water interaction study from hotspot region. *Int. J. Environ. Sci. Technol.* **2022**, *19*, 4891–4900. [CrossRef]
50. Misra, A.K.; Mishra, A. Study of quaternary aquifers in Ganga Plain, India: Focus on groundwater salinity, Fluoride and fluorosis. *J. Hazard. Mater.* **2007**, *144*, 438–448. [CrossRef]
51. Muhammad, S.; Shah, M.T.; Khan, S. Health risk assessment of heavy metals and their source apportionment in drinking water of Kohistan region, northern Pakistan. *Microchem. J.* **2011**, *98*, 334–343. [CrossRef]
52. Ground Water Department, Uttar Pradesh; Central Ground Water Board, Northern Region. *Dynamic Ground Water Resources of Uttar Pradesh*; Ground Water Department, Uttar Pradesh, and Central Ground Water Board: Lucknow, India, 2021.
53. Zhao, Z.; Kumar, A.; Wang, H. Predicting Arsenic Contamination in Groundwater: A Comparative Analysis of Machine Learning Models in Coastal Floodplains and Inland Basins. *Water* **2024**, *16*, 2291. [CrossRef]
54. Gupta, D.S.; Biswas, A.; Ghosh, P.; Rawat, U.; Tripathi, S. Delineation of groundwater potential zones, groundwater estimation and recharge potentials from Mahoba district of Uttar Pradesh, India. *Int. J. Environ. Sci. Technol.* **2021**, *19*, 12145–12168. [CrossRef]

55. Rahman, A. "Petrology and Geochemistry of Bundelkhand Granites Around Mahoba, Dist Hamirpur UP". Available online: https://core.ac.uk/download/pdf/144517481.pdf (accessed on 18 November 2024).
56. WHO. *Guidelines for Drinking-Water Quality: First Addendum to the Fourth Edition*; World Health Organization: Geneva, Switzerland, 2017.
57. *IS 10500*; Bureau of Indian Standards-Indian Standard Specification for Drinking Water. BIS: New Delhi, India, 2012.
58. Gibbs, R.J. Mechanisms controlling world water chemistry. *Science* **1970**, *170*, 1088–1090. [CrossRef] [PubMed]
59. Chadha, D.K. A proposed new diagram for geochemical classification of natural water and interpretation of chemical data. *Hydrogeol. J.* **1999**, *7*, 431–439. [CrossRef]
60. Cloutier, V.; Lefebvre, R.; Therrien, R.; Savard, M.M. Multivariate statistical analysis of geochemical data as indicative of the hydrogeochemical evolution of groundwater in a sedimentary rock aquifer system. *J. Hydrol.* **2008**, *353*, 294–313. [CrossRef]
61. Kumar, P.; Gupta, D.S.; Rao, K.; Biswas, A.; Ghosh, P. Delineation of groundwater potential zones and its extent of contamination from the hard rock aquifers in west-Bengal, India. *Environ. Res.* **2024**, *249*, 12145–12168. [CrossRef]
62. Kannojiya, P.K.; Raju, A.; Singh, A.; Srivastava, N.; Singh, S.; Singh, M. Health risk assessment from exposure to dissolved trace element concentration in drinking groundwater resources of Central Ganga Alluvial Plain: A case study of Lucknow region. *Urban Water J.* **2023**, *19*, 846–858. [CrossRef]
63. Ward, J.H. Ward's method. *J. Am. Stat. Assoc.* **1963**, *58*, 236–246. [CrossRef]
64. CIESIN. Documentation for the Gridded Population of the World, Version 4 (GPWv4), Revision 11 Data Sets. NASA Socioeconomic Data and Applications Center (SEDAC), Center for International Earth Science Information Network, Columbia University. 2018. Available online: https://data.nasa.gov/w/8nsk-ng4h/default?cur=q9bEB2fiVLf (accessed on 18 November 2024).
65. Piper, A.M. A graphical procedure in the geochemical interpretation of water analysis. *Am. Geophys. Union Trans.* **2007**, *25*, 119–129.
66. Datta, P.S.; Tyagi, S.K. Major ion chemistry of groundwater in Delhi area: Chemical weathering processes and groundwater flow regime. *Geol. Soc. India* **1996**, *47*, 179–188. [CrossRef]
67. Gaillardet, J.; Dupre, B.; Louvat, P.; Allegre, C.J. Global silicate weathering and $CO_2$ consumption rates deduced from the chemistry of large rivers. *Chem. Geol.* **1999**, *159*, 3–30. [CrossRef]
68. UNEPA. *Guidance for Performing Aggregate Exposure and Risk Assessments*; Office of Pesticide Programs: Washington, DC, USA, 1999.
69. Chen, J.; Wu, H.; Qian, H.; Gao, Y. Assessing nitrate and fluoride contaminants in drinking water and their health risk of rural residents living in a semiarid region of Northwest China. *Expo Health* **2017**, *9*, 183–195. [CrossRef]
70. Basu, A.K. Geology of parts of the Bundelkhand granite massif, Central India. *J. Geol. Soc. India* **1986**, *117*, 61e124.